




# Spiers Memorial Lecture: Towards understanding of iontronic systems: electroosmotic flow of monovalent and divalent electrolyte through charged cylindrical nanopores

Thiago Colla, <sup>a</sup> Igor M. Telles,<sup>b</sup> Muhammad Arfan,<sup>b</sup> Alexandre P. dos Santos <sup>b</sup> and Yan Levin <sup>\*b</sup>

Received 8th March 2023, Accepted 10th May 2023

DOI: 10.1039/d3fd00062a

In many practical applications, ions are the primary charge carrier and must move through either semipermeable membranes or through pores, which mimic ion channels in biological systems. In analogy to electronic devices, the “iontronic” ones use electric fields to induce the charge motion. However, unlike the electrons that move through a conductor, motion of ions is usually associated with simultaneous solvent flow. A study of electroosmotic flow through narrow pores is an outstanding challenge that lies at the interface of non-equilibrium statistical mechanics and fluid dynamics. In this paper, we will review recent works that use dissipative particle dynamics simulations to tackle this difficult problem. We will also present a classical density functional theory (DFT) based on the hypernetted-chain approximation (HNC), which allows us to calculate the velocity of electroosmotic flows inside nanopores containing 1:1 or 2:1 electrolyte solution. The theoretical results will be compared with simulations. In simulations, the electrostatic interactions are treated using the recently introduced pseudo-1D Ewald summation method. The zeta potentials calculated from the location of the shear plane of a pure solvent are found to agree reasonably well with the Smoluchowski equation. However, the quantitative structure of the fluid velocity profiles deviates significantly from the predictions of the Smoluchowski equation in the case of charged pores with 2:1 electrolyte. For low to moderate surface charge densities, the DFT allows us to accurately calculate the electrostatic potential profiles and the zeta potentials inside the nanopores. For pores with 1:1 electrolyte, the agreement between theory and simulation is particularly good for large ions, for which steric effects dominate over the ionic electrostatic correlations. The electroosmotic flow is found to depend very strongly on the ionic radii. In the case of pores containing 2:1 electrolyte, we observe a reentrant transition in which the electroosmotic flow first reverses and then returns to normal as the surface charge density of the pore is increased.

<sup>a</sup>Instituto de Física, Universidade Federal de Ouro Preto, Ouro Preto, MG, 35400-000, Brazil. E-mail: colla@ufop.edu.br

<sup>b</sup>Instituto de Física, Universidade Federal do Rio Grande do Sul, Caixa Postal 15051, Porto Alegre, RS, CEP 91501-970, Brazil. E-mail: alexandre.pereira@ufrgs.br; levin@ifufrgs.br

# 1. Introduction

There are numerous examples in which ion-solvent flow takes place in strongly confining environments – such as narrow channels,<sup>1–5</sup> nano-wires,<sup>6,7</sup> carbon nanotubes (CNTs)<sup>8–10</sup> or across porous media.<sup>11,12</sup> Such electroosmotic flows play a major role in transport phenomena important in many technological<sup>13–17</sup> and biological<sup>18–22</sup> applications. Examples range from osmotic equilibrium in living cells,<sup>23,24</sup> charge storage devices,<sup>25,26</sup> and solvent filtering<sup>27,28</sup> to desalination of seawater.<sup>29–33</sup> From a practical viewpoint, the transport of solvent through synthetic nanotubes can be optimized by adjusting the tube's molecular inner structure. This can facilitate solvent flow while avoiding the passage of ions,<sup>34</sup> thus resulting in efficient salt filtering. On the other hand, ion transport through ion channels is of fundamental importance in many biological processes, such as the propagation of electrical signals in nervous systems<sup>35,36</sup> and electrical stimuli in muscle cells.<sup>37</sup> The action potential across the cell membrane<sup>38–40</sup> is controlled by selectivity filters, which can block the passage of some ions while allowing the passage of others.<sup>20,28,41–43</sup> One of the reasons for the selectivity of ion channels is the dehydration of ions upon entering the nanopore.<sup>44,45</sup> This dehydration is the result of interaction of ions with the proteins of the selectivity filter. Moreover, specific ion interactions with the channel inner walls are also known to play a crucial role in determining the dynamics of their transport along the channel.<sup>29,46,47</sup> In all these cases, solvent and ion motion through the pore depend crucially on the interactions of particles with the surface.<sup>48</sup> In analogy to electronic devices, the “iontronic” ones use electric fields to induce charge motion that results in the delivery of precise amounts of substances, which can be biomolecules, ions, or pharmaceuticals, to specific locations. In spite of its enormous practical relevance, the theoretical description of transport phenomena through narrow cylindrical pores remains poorly understood,<sup>49,50</sup> and many open questions must still be elucidated.<sup>51</sup> The difficulties arise from the inherently interfacial nature of such systems, typical of strongly confined environments, for which traditional theoretical tools designed for bulk systems<sup>52,53</sup> do not directly apply.<sup>54,55</sup>

Ion transport through narrow pores takes place whenever a gradient in pressure,<sup>56–58</sup> concentration<sup>2,59–61</sup> or electric potential<sup>62–64</sup> is established across the tube's longitudinal length. If the channel connects two microscopic volumes, the ions and solvent flow can be characterized as a transient state that lasts until an equilibrium condition of zero gradient of electrochemical potential is established across the channel and the flow ceases to exist. On the other hand, a stationary state of non-vanishing ion flux can be established *via* an active process in which an applied force drives the ion flow along the channel connecting two mesoscopic or macroscopic volumes. When the driving force for the flow is the electric field across the longitudinal direction of the pore, the resulting ion-solvent motion is denoted as the electroosmotic flow.<sup>2,60,65</sup> Even though the applied electric field does not couple directly to the solvent dipoles, the motion of ions will partially transfer their momentum to the solvent molecules through particle collisions, resulting in solvent motion. If the pore surface is charged, the moving ions will be further subjected to a radial static field produced by the dissociated charge on the pore surface.

Simulation of such charged systems is a highly non-trivial task. The long-range nature of the Coulomb force precludes the interaction between particles being simply cut off at the boundary of the simulation box using the minimum image convention, standard for systems with short-range interactions. Instead, one needs to construct a periodic replication of the simulation box so that the force felt by a given ion arises not only from the other ions inside the simulation box, but also from their infinite periodic replicas. For bulk systems, the summation over replicas can be efficiently performed using Ewald methods;<sup>66</sup> however, if the periodicity of the simulation box extends only in two (slab geometry) or one (cylindrical geometry) dimension, additional corrections must be included in 3D Ewald summation method.<sup>67,68</sup> Recently, dissipative particle dynamics (DPD)<sup>69,70</sup> simulations have been proposed to investigate electroosmotic flows through narrow channels, combining both the Green function formalism<sup>64,71,72</sup> and the Ewald summation to efficiently account for the electrostatic interactions between infinite numbers of replicas in a cylindrical geometry.<sup>73</sup> Embedding of a pore into a medium of an arbitrary dielectric constant, such as a cell membrane, is taken into account using the Green function formalism.<sup>74</sup> Since a uniform surface charge does not produce any electric field inside an infinite cylindrical pore, it can be neglected for the calculation of the force acting on each ion. However, if this is done, the pore will no longer be charge-neutral. The traditional approach is to use point surface charges to account for the pore's surface charge density, keeping the overall charge neutrality of the pore + surface system. This, however, is very inefficient, since one must include the surface point charges inside the Ewald summation. To overcome these difficulties, one can use an implementation of the Ewald summation method for charge-non-neutral systems.<sup>64</sup> This method only requires a small modification of the total electrostatic energy of the replicated system and is significantly more efficient than the point charge approach.

The surface-ion interactions result in radial dependence of the flow along the cylinder. Of particular interest is the radial distance at which the ion average velocity vanishes – the so-called shear plane – and the associated electrostatic potential, known as the zeta potential.<sup>75</sup> The zeta potential can be related to the flow velocity at the center of the pore using the Smoluchowski equation.<sup>76–78</sup> Under some conditions, it is possible to find a reversal of the electrophoretic mobility,<sup>79</sup> characterized by the change in the direction of the fluid flow. This effect can be attributed to the reversal of the surface charge near the pore surface – the counterion condensation that overcompensates the surface charge.<sup>52,80</sup> As a result, the effective surface charge of the pore becomes reversed. From the overall charge neutrality, this means that the net charge of free (*i.e.*, uncondensed) ions available to respond to the external field also reverses sign, resulting in the reversal of the electroosmotic flow.

If the external electric field is not too large, the Smoluchowski equation can be used to relate the fluid velocity with the zeta and electrostatic potential.<sup>81</sup> However, application of the Smoluchowski equation requires knowledge of the location of the shear plane and of the electrostatic potential inside the pore. At the moment there is no theoretical method available to locate the position of the shear plane. However, within the DPD formalism, it can be easily calculated using an independent salt-free simulation of a pressure- or gravity-driven flow through a cylindrical pore.<sup>82</sup> On the other hand, theoretical calculations of the electrostatic potential inside a strongly charged pore containing multivalent counterions, the

characteristic regime for which reversal of the electroosmotic flow takes place,<sup>82</sup> are rather challenging. The traditional Poisson–Boltzmann (PB) equation is able to accurately predict the distribution of monovalent,<sup>83–85</sup> point-like ions close to a moderately charged surface,<sup>86</sup> but fails<sup>50,87–89</sup> to capture the effects of electrostatic correlations present inside the double layer in the strong coupling regime, or when packing effects become important. To overcome these difficulties, in the present paper we will use a new density functional theory (DFT), designed to accurately describe both strong electrostatic and size correlations inside the double layer close to the cylindrical pore surface.<sup>90</sup>

Classical DFT is a powerful tool to predict the equilibrium distribution of microscopic particles subject to external fields. It is particularly suitable for studying interfacial phenomena with a high degree of accuracy,<sup>53,91–95</sup> yet with a reasonably low computational cost in comparison to most computer simulations.<sup>96,97</sup> Another clear advantage of the DFT formalism is the possibility of treating various contributions to the free energy using different levels of approximations.<sup>98–100</sup> The key idea is to construct a free-energy functional that accounts for the electrostatic and steric interactions inside an inhomogeneous fluid, and then subject it to the stationary (Euler–Lagrange) condition in order to obtain the desired equilibrium profiles (usually through a set of coupled integral equations).<sup>101,102</sup> While ideal contributions to the free-energy functional are known exactly, contributions from different inter-particle interactions (the so-called excess contributions) beyond the mean-field are unknown, requiring the employment of approximations that must account for the correlational effects. Depending on the particular system regime and/or the nature of the inter-particle interactions, some contributions can be handled at the mean-field level<sup>103,104</sup> or through simple local approximations, while other relevant contributions can be treated separately using more sophisticated approaches.<sup>93</sup> One classical example is the hard-sphere interactions and the underlying packing effects, which are known to be very accurately described by the Rosfeld fundamental measure theory<sup>105–107</sup> (FMT) and its various extensions,<sup>107–111</sup> up to very high packing fractions and degrees of polydispersity. The theory is based on the classical weight-density approximation,<sup>112</sup> whereby the weighting densities are chosen so as to incorporate some key geometrical features of overlapping particles, and the local free energy is constructed so as to reproduce the correct dimensional crossover, as well as to satisfy some prescribed properties in the bulk limit.<sup>53,107</sup> The remaining interactions can be treated in a number of different approaches, depending on the desired degree of accuracy. Traditional approaches involve, for example, the use of either weighted<sup>113–116</sup> or local<sup>117–119</sup> concentrations in a known free-energy density of a related bulk fluid, functional expansions about a reference (either non-uniform or bulk) system,<sup>120–122</sup> gradient expansions,<sup>91,123</sup> or the introduction of coupling parameters that allow one to continuously change the equilibrium properties from a known reference state to the final one.<sup>53,124–126</sup> In the case of electrostatic correlations, solutions of the mean spherical approximation (MSA)<sup>124,127,128</sup> for the bulk ion correlations are often employed in a combination with the methods mentioned above. The great advantage of the MSA is that closed analytical formulae for the key thermodynamic quantities and pair correlations of the bulk fluid (usually required as inputs in the DFT formalism) are known, which greatly facilitates the numerical implementation of these methods.<sup>129–132</sup> However, the MSA relation loses its accuracy in the case of strong electrostatic couplings,

since it neglects the non-linear correlations that become relevant in these regimes.<sup>133–135</sup> An alternative is to rely on the hypernetted-chain (HNC) closure relation<sup>136</sup> (which does incorporate non-linear effects) for computing the underlying bulk properties. Although the use of the HNC approach requires numerical solutions of the Ornstein–Zernike (OZ) integral equations, these solutions are expected to be considerably more accurate in capturing strong ion correlations than their MSA counterparts.<sup>137,138</sup> In spite of additional computation cost, this gain in accuracy might represent a good compromise whenever fine details of equilibrium distributions close to interfaces are required, as is the case for the calculation of the zeta potential close to a highly charged pore surface.

In this work, the theoretical tools described above (DPD simulations and classical DFT) are combined to investigate the electroosmotic flow along an infinite cylindrical channel, driven by a static electric field. A DFT method is proposed that uses the Percus particle-insertion idea to compute the local excess chemical potential in the framework of the HNC approach.<sup>139–141</sup> These chemical potentials are then evaluated over all the grid points using suitable weighted densities, thus allowing us to calculate the equilibrium profiles in a self-consistent fashion. The method is then applied to calculate zeta potentials that characterize the electroosmotic flow through charged cylinders, and compared with the results of the DPD simulation. Different combinations of ionic charges and sizes are considered, and a good agreement between DFT and simulation results is found in all cases. Our simulations show that in the case of divalent ions, reversal of electroosmotic flow always takes place after the pore-surface charge density reaches a threshold value, clearly indicating charge reversal produced by the condensation of divalent counterions close to the pore surface. Increasing the ionic size makes the electroosmotic flow reverse back to its normal direction after a sufficiently large surface charge is reached. This behavior can be understood to be a consequence of steric repulsion between the counterions that prevents the critical number of counterions needed to reverse the pore surface charge from packing close together within the shear plane.

The remaining part of the paper is organized as follows. In Section 2, the model system and the applied DPD simulations are described. The Smoluchowski equation is derived in Section 3. An overview of the DFT formalism used to compute equilibrium distributions and zeta potentials is provided in Section 4. Results are then presented and discussed in detail in Section 5, followed by the closing remarks and perspectives for further investigations discussed in Section 6. Finally, specific details regarding the DFT calculations and implementation are presented in the Appendices.

## 2. Model and simulations

Consider a cylindrical pore of radius  $R$ , length  $L$  and uniform surface charge density  $\sigma < 0$ , as depicted in Fig. 1. Inside the cylinder there are  $N_{\text{sol}}$  solvent and  $N$  charged particles. Periodic boundary conditions are applied along the longitudinal  $z$ -direction. The no-slip boundary condition is implemented using the bounce-back method<sup>142</sup> at  $r = R - r_i$ , where  $r_i$  is the effective ionic radius. The  $N$  charged particles consist of  $N_+$   $\alpha$ -valent cations (counterions) and  $N_-$  monovalent anions (coions). The total ionic charge at the pore wall is  $-2\pi RL\sigma$ . The “bulk” concentration of an  $\alpha:1$  salt is defined as the concentration in the center of the

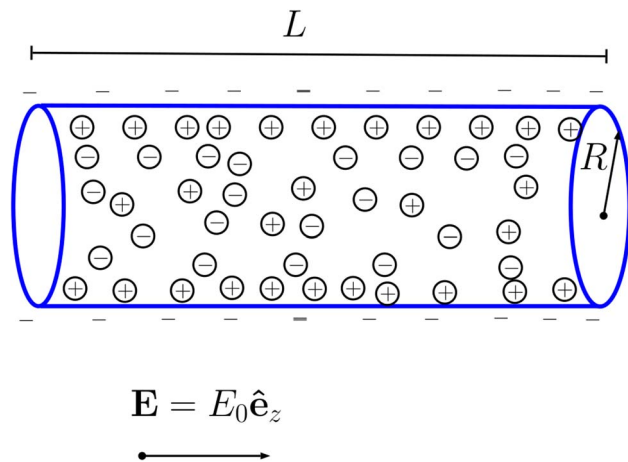


**Fig. 1** A sketch of the system. A hollow cylinder, bearing a negative uniform surface charge density  $\sigma$ , has radius  $R$  and length  $L$ . It contains ions of radius  $r_i$  and charge  $q_+ = \alpha e$  and  $q_- = -e$ , as well as soft DPD particles representing solvent (not shown in the figure). In our simulations, a static electric field is applied along the longitudinal axis leading to an electroosmotic flow. The cylinder is inside a simulation box with periodic boundary conditions, whose transversal dimensions are much larger than  $L$ . A 3D Ewald method with a correction term, which accounts for the preferential  $z$ -wise summation and for the lack of charge neutrality inside the pore,<sup>82</sup> is used to treat all the electrostatic interactions between the ions. In the DFT calculations, the limit  $L \rightarrow \infty$  is implicitly considered.

pore at  $r = 0$ ,  $\rho^0 = 0.025l_B^{-3}$  (where  $l_B$  is the Bjerrum length), which gives around 112 mM. We note that in addition to cations derived from salt dissociation, there are  $N_c = 2\pi RL|\sigma|/\alpha e$  counterions present to neutralize the surface charge, where  $e$  is the elementary charge of a proton. These additional counterions are the result of dissociation of the surface groups.

The simulations are performed using the DPD method,<sup>69</sup> which consists of conservative, friction, and random forces acting on each particle in such a way as to respect the fluctuation–dissipation theorem and the conservation of momentum in order to achieve the hydrodynamic limit with a small number of solvent particles. The simulations are carried out inside a cylinder of  $R = L = 10l_B$ , considering the solvent as water at room temperature. Within the DPD formalism,<sup>69</sup> a solvent particle does not correspond to an individual water molecule, but rather to a cluster of  $N_w$  water molecules, which are treated as soft spheres of radius  $r_c$ . The natural unit of length for the simulations is the Bjerrum length,  $l_B = e^2\beta/\epsilon = 7.2 \text{ \AA}$ , where  $\beta = 1/k_B T$  and  $k_B$  is the Boltzmann constant,  $T$  is the temperature and  $\epsilon$  is a uniform dielectric constant over all space – inside and outside the pore. We will set the size of the pseudo-solvent particles to be  $r_c = l_B$ . The number of these particles inside the pore is  $N_{\text{sol}}$ , with the average concentration set to  $n_{\text{sol}} = 4l_B^{-3}$ . On average, in bulk, a water molecule occupies  $30 \text{ \AA}^3$  of volume, which means that a pseudo-particle contains 3 water molecules. The effects of the dielectric discontinuity across the pore surface can be added using the Green function formalism developed in ref. 74. Both solvent and ions are considered with the same mass  $m$  and all other DPD parameters are the same as in the earlier work.<sup>82</sup> The electrostatic energy is calculated using a 3D Ewald

summation method, corrected for a pseudo-1D geometry inside the pore.<sup>73</sup> The cylinder is placed along the minor axis of a rectangular simulation box of sides  $L_p \times L_p \times L$ , with periodic boundary conditions in the  $z$ -direction. Outside the pore, the simulation contains empty space. This empty space is necessary because the 3D Ewald method creates spurious replicas of the pore in all 3 dimensions. The value  $L_p = 4R$  allows the formation of an empty space outside the cylinder, necessary to avoid the interaction between the undesired periodic replicas along the  $x$  and  $y$ -directions. The electrostatic force acting on each ion can be calculated from the gradient of the electrostatic energy.<sup>82</sup> Additionally to the DPD and electrostatic forces, a truncated Lennard-Jones potential<sup>143</sup> with  $\sigma_{LJ} = 2r_i$ , strength  $\varepsilon_{LJ} = 2\beta^{-1}$  and cutoff radius  $r_{LJ} = 2^{1/6}\sigma_{LJ}$  is included in the interactions between all charged particles. The electroosmotic flow is induced by an external electric field  $E_0 = 1(\beta e l_B)^{-1}$  applied in the  $+z$ -direction, leading to a force  $\mathbf{F}_z = q_i E_0 \hat{\mathbf{z}}$  on an ion  $i$ . Note that the electric fields used in computational simulations are much stronger than the typical experimental fields, which would induce very weak currents, similar to the numerical error in simulations. In the regimes studied in the present paper, the induced flows are linearly proportional to the external field, so that the corresponding flows under the experimental conditions can be easily obtained by a simple scaling. The integration of the equations of motions is implemented using the Velocity-Verlet algorithm.<sup>144</sup> The statistical analysis is performed over  $5 \times 10^4$  samples obtained each 10 time steps, after a stationary flow is established, which takes approximately  $5 \times 10^5$  time steps.

### 3. Smoluchowski equation

When a static electric field is applied along the pore axis, a steady current is established after a transitory period. From symmetry, the stationary velocity profile depends only on the radial distance from the cylinder's major axis. In a cylindrical geometry, the Stokes equation reduces to<sup>82</sup>

$$0 = E_0 \varrho_q + \eta \nabla^2 v \quad (1)$$

where  $\eta$  is the dynamic viscosity and  $v$  is the  $z$  component (along the major axis of the cylinder) of the fluid velocity. The ionic charge density  $\varrho_q$  is defined as  $\varrho_q = \sum \alpha_i e \rho_i$ , where  $\rho_i$  is the local concentration of ionic species  $i$ , and is related to the electrostatic potential  $\phi(S)$  by the Poisson equation:

$$\nabla^2 \phi(S) = -\frac{4\pi}{\varepsilon} [\sigma \delta(S - R) + \varrho_q(S)], \quad (2)$$

where  $S$  is the radial distance measured from the center of the pore and  $\delta$  represents the Dirac delta function. Combining eqn (1) and (2), we obtain the Smoluchowski equation,

$$v(S) = \frac{\varepsilon E_0}{4\pi\eta} (\phi(S) - \zeta), \quad (3)$$

where we have defined the electrostatic potential at the shear plane as  $\phi(S_{sh}) \equiv \zeta$ . The location of the shear surface is defined as the radial position at which the fluid velocity vanishes,  $v(S_{sh}) = 0$ . The DPD simulations allow us to calculate the fluid velocity in the center of the pore  $v(0)$  – see Fig. 3. Setting the electrostatic

potential at the center of the pore to be zero, we can use the fluid velocity at the center of the pore and eqn (3) to calculate the zeta potential,

$$\zeta = -\frac{4\pi\tilde{\eta}\tilde{v}(0)}{\tilde{E}_0}, \quad (4)$$

where  $\tilde{\eta} = \eta(\beta/m)^{0.5}l_B^2$ ,  $\tilde{E}_0 = \beta ql_B E_0$ , and the reduced velocity is defined as  $\tilde{v} = v(m\beta)^{0.5}$ . The reduced dynamic viscosity for our system can be calculated using a separate DPD simulation of a simple Poiseuille flow,<sup>145</sup> yielding  $\tilde{\eta}=1.13$ . We should note that with the natural time scale of our simulations  $\tau_0 = l_B\sqrt{m\beta}$  the characteristic viscosity is about two orders of magnitude smaller than that of water. It is easy to rescale the characteristic time, so as to get the exact value of viscosity of water; however, this will perturb other properties, such as the electric field, diffusivity, and velocity of ions. There is a large part of the DPD community working on a way to adjust various parameters in the conservative and dissipative parts of force in the DPD algorithm to properly describe various aspects of solutions, and in particular to get the correct Schmidt number. In our case, however, we shall not worry about these complications, since our goal is to test the Smoluchowski equation, which for the pore geometry should be valid for an arbitrary solvent viscosity. The value of  $\zeta$  obtained using eqn (4) can be compared with an independent calculation of the electrostatic potential at the location of the shear plane. To do this, we will now proceed to construct a DFT theory that will allow us to accurately calculate the ionic distributions inside the pore.

## 4. Density functional theory

As discussed above, the fluid velocity profile can be related with the equilibrium electrostatic potential *via* the Smoluchowski equation. The electrostatic potential can in turn be computed once the equilibrium profiles are known, *e.g.* by a simple application of the Gauss law. In order to compute the equilibrium profiles, we shall here employ the DFT formalism for the model system described above. We begin by writing the equilibrium grand potential as a combination of different functionals:

$$\Omega[\{\rho_i(\mathbf{r})\}] = \mathcal{F}_{\text{id}}[\{\rho_i(\mathbf{r})\}] + \mathcal{F}_{\text{ex}}[\{\rho_i(\mathbf{r})\}] + \sum_i \int (\phi_i(\mathbf{r}) - \mu_i)\rho_i(\mathbf{r})d\mathbf{r}, \quad (5)$$

where  $\{\rho_i(\mathbf{r})\}$  denotes the collection of density profiles of the various confined species,  $\mathcal{F}_{\text{id}}$  and  $\mathcal{F}_{\text{ex}}$  denote the ideal gas and excess (over ideal) free-energy functionals, respectively,  $\mu_i$  is the reservoir chemical potential of component  $i$ , and  $\phi_i(\mathbf{r})$  is the external (surface) potential acting on species  $i$  and is composed of an electrostatic contribution,  $\phi_i^{\text{el}}(\mathbf{r})$ , in addition to the hard repulsion potential,  $\phi_i^{\text{hs}}(\mathbf{r})$ , at wall-ion contact. The ideal gas contribution is

$$\mathcal{F}_{\text{id}}[\{\rho_i(\mathbf{r})\}] = k_B T \sum_i \int \rho_i(\mathbf{r}) (\log(\Lambda^3 \rho_i(\mathbf{r})) - 1) d\mathbf{r}, \quad (6)$$

where  $\Lambda$  denotes the thermal wavelength. The excess free-energy,  $\mathcal{F}_{\text{ex}}$ , contains the contributions from all particle interactions. It is convenient to further split this quantity into hard-sphere and electrostatic contributions,  $\mathcal{F}_{\text{ex}} = \mathcal{F}_{\text{hs}} + \mathcal{F}_{\text{el}}$ . The hard-sphere contribution is known to be accurately described by the FMT



formalism, where it is written in terms of a local free energy density  $\Phi[n_\alpha(\mathbf{r})]$  as<sup>106,107</sup>

$$\mathcal{F}_{\text{hs}}[\{\rho_i(\mathbf{r})\}] = \int \Phi[\{n_\alpha(\mathbf{r})\}] d\mathbf{r} \quad (7)$$

The quantities  $n_\alpha(\mathbf{r})$  are obtained as weighted averages over the particle profiles,

$$n_\alpha(\mathbf{r}) = \sum_i \int \rho_i(\mathbf{r}') \omega_i^{(\alpha)}(\mathbf{r} - \mathbf{r}') d\mathbf{r}', \quad (8)$$

where  $\omega_i^{(\alpha)}(\mathbf{r} - \mathbf{r}')$  are a set of suitable weighting functions (either scalar or vector fields) that depend on the geometry of the overlapping particles. In the case of hard-spheres, these quantities correspond to four scalar functions  $\omega_i^{(3)}(R) = \Theta(r_i - R)$ ,  $\omega_i^{(2)}(R) = \delta(R - r_i)$ ,  $\omega_i^{(1)}(R) = \omega_i^{(2)}(R)/4\pi r_i$  and  $\omega_i^0(R) = \omega_i^{(1)}(R)/4\pi r_i^2$ , and two vector functions  $\omega_i^{(2)}(R) = -\nabla \omega_i^{(3)}(R) = \delta(R - r_i) \hat{\mathbf{e}}_R$  and  $\omega_i^{(1)}(R) = \omega_i^{(2)}(R)/4\pi r_i$ . Here,  $\Theta$  denotes the Heaviside step-function, which vanishes if  $x < 0$  and equals one otherwise and  $R = |\mathbf{r} - \mathbf{r}'|$ ,  $r_i$  is the radius of particle component  $i$ , and  $\hat{\mathbf{e}}_R$  denotes a unit vector pointing in the direction of  $\mathbf{r} - \mathbf{r}'$ . Due to the translational symmetry along the longitudinal direction  $z$  and the azimuthal symmetry around the principal axis of the pore, the equilibrium profiles only depend on the radial distance  $S$  from the cylinder center. It follows that the integrals over both the azimuthal angle  $\varphi$  and the longitudinal coordinate  $z$  can be performed explicitly. The detailed calculations can be found in Appendix A. Here, we apply the White-Bear version of the FMT, in which the free energy density is given by<sup>107,109,110</sup>

$$\beta\Phi[\{n_\alpha(\mathbf{r})\}] = -n_0 \ln(1 - n_3) + \frac{n_1 n_2 - \mathbf{n}_1 \cdot \mathbf{n}_2}{(1 - n_3)} + \frac{n_2^3 - 3n_2 \mathbf{n}_1 \cdot \mathbf{n}_2}{36\pi n_2^3 (1 - n_3)^2} \times [n_3 + (1 - n_3)^2 \ln(1 - n_3)]. \quad (9)$$

This functional was constructed to correctly reproduce the Mansoori–Carnahan–Starling–Leland (MCSL) equation of state in the bulk limit.<sup>146</sup>

The electrostatic functional  $\mathcal{F}_{\text{el}}$  can be separated into mean-field and residual functionals,  $\mathcal{F}_{\text{el}} = \mathcal{F}_{\text{mf}} + \mathcal{F}_{\text{res}}$ , the latter containing all effects from the electrostatic correlations, which are fully neglected in the mean-field contribution. The mean-field functional reads

$$\mathcal{F}_{\text{mf}} = \frac{e^2}{2\epsilon} \sum_{ij} \int \frac{\alpha_i \alpha_j \rho_i(\mathbf{r}) \rho_j(\mathbf{r}')}{|\mathbf{r} - \mathbf{r}'|} d\mathbf{r} d\mathbf{r}', \quad (10)$$

where the sum is performed over all ionic species. This contribution can be clearly recognized as the electrostatic energy arising from ion interactions, if their positional correlations are ignored. It is convenient to combine this contribution with the ion-surface Coulomb interactions present in the last term of eqn (5):

$$\sum_i e \alpha_i \int \phi_i^{\text{el}}(\mathbf{r}) \rho_i(\mathbf{r}) d\mathbf{r} = \sum_i \frac{e^2}{\epsilon} \int \frac{\alpha_i \rho_i(\mathbf{r}) q_{\text{pore}}(\mathbf{r}')}{|\mathbf{r} - \mathbf{r}'|} d\mathbf{r} d\mathbf{r}', \quad (11)$$

where  $\varrho_{\text{pore}}(\mathbf{r}') = \sigma\delta(S' - R)$  is the cylinder surface charge density. We thus arrive at the total mean-field electrostatic contribution given by:

$$\mathcal{F}_{\text{coul-mf}} = \frac{e}{2} \sum_i \alpha_i \int \rho_i(\mathbf{r}) \psi(\mathbf{r}) d\mathbf{r}, \quad (12)$$

where  $\psi(\mathbf{r})$  denotes the mean-field averaged electrostatic potential inside the cylinder:

$$\psi(\mathbf{r}) = \frac{e}{\varepsilon} \int \left( \sum_i \alpha_i \rho_i(\mathbf{r}') + \varrho_{\text{pore}}(\mathbf{r}') \right) \frac{d\mathbf{r}'}{|\mathbf{r} - \mathbf{r}'|}. \quad (13)$$

Since the ionic density distributions depend only on the radial distance, the averaged potential will clearly possess the same symmetry. Performing the integration over the azimuthal angle  $\varphi'$  and the longitudinal coordinate  $z'$ , one finds

$$\psi(S) = \frac{4\pi e}{\varepsilon} \sum_i \alpha_i \int_0^S \ln\left(\frac{S'}{S}\right) \rho_i(S') S' dS', \quad (14)$$

where we have set the potential to vanish at the center of the cylinder. Note that the surface charge does not contribute explicitly to the internal potential (apart from an arbitrary shift), a fact that could have been anticipated based on the Gauss law and symmetry considerations. Its contribution is, however, implicitly accounted for by the lack of electroneutrality of the confined ions, whose charge must balance the charge on the pore surface.

The only contribution left in eqn (5) is the residual contribution  $\mathcal{F}_{\text{res}}$ , which accounts for the electrostatic correlations. Instead of calculating this contribution explicitly, we shall here adopt a different approach, in which the corresponding chemical potentials will be evaluated in the context of the HNC approach, as shown below. Application of the Euler-Lagrange condition  $\frac{\delta\Omega}{\delta\rho_i(\mathbf{r})} = 0$  to the functional eqn (5) then yields

$$\rho_i(S) = \rho_i^0 \exp(-\beta\alpha_i\psi(S) - \mu_i^{\text{hs}}(S) - \mu_i^{\text{res}}(S)) \quad (15)$$

for  $S \leq R - r_i$ , and  $\rho_i(S) = 0$  for  $S > R - r_i$ . The latter condition is due to the hard-core ion-surface interactions. In the relation above,  $\rho_i^0 = \frac{e^{\beta\mu_i}}{\Lambda^3}$  are the particle activities in the reservoir which is implicitly in contact with the system. In practice, these concentrations are adjusted to provide the desired “bulk” concentrations far away from the surface, at  $S = 0$ . The hard-sphere and residual chemical potentials are defined as  $\mu_i^{\text{hs}}(S) = \frac{\delta\mathcal{F}_{\text{hs}}}{\delta\rho_i(S)}$  and  $\mu_i^{\text{res}}(S) = \frac{\delta\mathcal{F}_{\text{res}}}{\delta\rho_i(S)}$ , respectively. The former quantity can be readily evaluated from eqn (7) to be:

$$\mu_i^{\text{hs}}(S) = \sum_{\alpha} \int \frac{\partial\Phi}{\partial n_{\alpha}(\mathbf{r}')} \omega_i^{(\alpha)}(\mathbf{r}' - \mathbf{r}) d\mathbf{r}'. \quad (16)$$

Again, we emphasize that, due to rotational and translation symmetries across the longitudinal axis, the integration above is a function of the radial coordinate  $S$  alone (see Appendix A).

In order to calculate the residual ionic contribution  $\mu_i^{\text{res}}(S)$ , we adopt an approach first introduced by Percus, in which the addition of a particle at some location of an otherwise uniform fluid is considered as the source of an external field. This allows for the application of the tools of classical DFT for computing equilibrium distributions and free-energy changes, which in this case can be directly assigned to pair correlation functions and excess chemical potentials, respectively, of the corresponding uniform system. Our strategy here is to relate the quantity  $\mu_i^{\text{res}}(\mathbf{r})$  to the free-energy change upon adding a particle in a uniform system whose concentrations can be identified as suitable average concentrations at point  $\mathbf{r}$ . The physical picture behind this idea is that the insertion of an ion at a given point will induce a polarization cloud in its vicinity, which comes at the expense of an energy fluctuation. Alternatively, the energy change upon particle insertion can be identified as the work that must be done in order to bring the particle from infinity up to its actual position – the so-called potential of mean force. In the context of the HNC approach, the change in excess free energy when an ion is inserted into an otherwise uniform electrolyte is (see Appendix B):

$$\beta\mu_i^{\text{ex}} = \frac{1}{2} \sum_j \rho_j^0 \int \left( 1 + \frac{h_{ij}(\mathbf{r})}{2} \right) \Gamma_{ij}^{\text{sr}}(\mathbf{r}) d\mathbf{r} - \beta\Delta\psi_i, \quad (17)$$

where  $h_{ij}(\mathbf{r})$  are total correlation functions,  $\Gamma_{ij}^{\text{sr}}(\mathbf{r}) \equiv h_{ij}(\mathbf{r}) - c_{ij}^{\text{sr}}(\mathbf{r})$ , with  $c_{ij}^{\text{sr}}(\mathbf{r}) = c_{ij}(\mathbf{r}) + \frac{l_B \alpha_i \alpha_j}{r}$  being the short-range contribution of the direct pair correlations  $c_{ij}(\mathbf{r})$ , and  $\beta\Delta\psi_i \equiv \beta\psi_i - \beta\psi_i^0 = l_B \sum_j \rho_j^0 \alpha_j \int \frac{h_{ij}(\mathbf{r})}{r} d\mathbf{r}$  is a density-dependent correlation potential – the change in electrostatic potential induced by the polarizing cloud upon insertion of an ion of species  $i$ . These quantities are related *via* the Ornstein–Zernike equation,

$$\Gamma_{ij}(\mathbf{r}) = \sum_k \rho_k^0 \int \Gamma_{ik}(\mathbf{r}') c_{kj}(|\mathbf{r} - \mathbf{r}'|) d\mathbf{r}', \quad (18)$$

where  $\Gamma_{ij}(\mathbf{r}) = h_{ij}(\mathbf{r}) - c_{ij}(\mathbf{r}) = \Gamma_{ij}^{\text{sr}} - \frac{\alpha_i \alpha_j l_B}{r}$ . This equation is to be supplemented by the HNC closure relation,

$$c_{ij}(\mathbf{r}) = e^{-\beta u_{ij}(\mathbf{r}) + \Gamma_{ij}(\mathbf{r})} - \Gamma_{ij}(\mathbf{r}) - 1 \quad (19)$$

allowing for the unique determination of the two unknowns  $c_{ij}(\mathbf{r})$  and  $\Gamma_{ij}(\mathbf{r})$ . Now, eqn (17) can be used to estimate the residual chemical potential in the context of a local-density approximation, in which the bulk concentrations  $\rho_j^0$  are replaced by the corresponding local equilibrium profiles,  $\rho_j^0 \rightarrow \rho_j(\mathbf{r})$ . The quantities  $\mu_i^{\text{ex}}(\mathbf{r})$  would in that case be local functionals of the density distributions. However, such local DFTs are inaccurate or even unstable in the case of strongly charged surfaces, when the local density profiles undergo strong spatial variations. A more appropriate approach is to consider the free energy to be a functional of weighted densities:

$$n_i(\mathbf{r}) = \int \rho_i(\mathbf{r}') \omega_i(\mathbf{r} - \mathbf{r}') d\mathbf{r}' \quad (20)$$

where the weighted functions  $\omega_i(\mathbf{r})$  are normalized to unity, in such a way as to recover the uniform densities in the bulk regime. We take the weighting functions to be  $\omega_i(\mathbf{r}) = \frac{3}{4\pi R_i^3} \Theta(r - R_i)$ , where  $R_i = r_i + \xi/2$ , and  $\xi = \left(4\pi l_B \sum_i \rho_i \alpha_i^2\right)^{-1/2}$  is the local Debye length at a given point – see the discussion in Appendix B. The residual chemical potentials are then evaluated in a self-consistent fashion as follows. First, a set of guess functions  $\rho_i(\mathbf{r})$  is introduced (*e.g.*, *via* solutions of the mean-field PB equation) and used in eqn (20) to evaluate the corresponding set of weighted densities. At each observation point  $\mathbf{r}$ , eqn (18) and (19) are numerically solved (under the replacement  $\rho_j^0 \rightarrow \eta_j(\mathbf{r})$ ) to provide the corresponding functions  $c_{ij}(\mathbf{r})$  and  $\Gamma_{ij}^{\text{st}}(\mathbf{r})$ , which now become functionals of the equilibrium densities. The excess chemical potentials are then computed *via* eqn (17) at each grid point  $\mathbf{r}$ . Note that the pair interactions  $u_{ij}(\mathbf{r})$  in eqn (19) comprise both electrostatic and hard-sphere interactions, and as a result the excess chemical potential also contains contributions from hard-sphere correlations. Since these contributions are already accounted for in eqn (16), they have to be removed from eqn (17) to avoid double-counting. This is done by evaluating this quantity for a uncharged system ( $q_i = 0$ ) of same concentrations. The resulting excess chemical potentials only contain electrostatic correlation effects, and can be readily identified with the residual chemical potentials  $\mu_i^{\text{res}}$  in eqn (15). After calculating the electrostatic potential and hard-sphere chemical potentials from eqn (14) and (16), respectively, new profiles can be obtained from eqn (15). The process is then repeated until convergence is achieved, following an optimized estimation method described in ref. 147.

In order to test the relevance of electrostatic correlations for ionic distributions inside charged pores – as well as the performance of different approaches in accounting for electrostatic correlations – we show in Fig. 2 comparisons between computer simulations and DFT approaches with different levels of approximation. Apart from the proposed weighted-HNC approach (red curves), we also show results in which the electrostatic correlations are fully neglected (amounting to set  $\mu_i^{\text{res}} = 0$ , see black curves), as well as predictions from a functional expansion around the bulk electrolyte in which the MSA approach is used to compute electrostatic correlations. In the latter case, the residual electrostatic correlations are computed *via* the following expression:

$$\beta\mu_i^{\text{res}}(\mathbf{r}) = \beta\mu_{0i}^{\text{res}} + \sum_j \int c_{ij}^0(|\mathbf{r} - \mathbf{r}'|) \delta\rho_j(\mathbf{r}') d\mathbf{r}', \quad (21)$$

where  $\mu_{0i}^{\text{res}}$  are the bulk residual chemical potentials, while  $c_{ij}^0(|\mathbf{r} - \mathbf{r}'|)$  are the electrostatic contributions to the bulk direct correlations (computed in the framework of the MSA approximation) and  $\delta\rho_j(\mathbf{r}') = \rho_j(\mathbf{r}') - \rho_j^0$  represent the first-order deviations from bulk distributions. Eqn (21) follows directly from a functional expansion of the excess free-energy around a reference bulk fluid. The resulting bulk-MSA approach has been widely applied as a robust DFT approach due to its reasonable accuracy and ease of implementation.

It is clear from Fig. 2 that the electrostatic correlations in the case of 2:1 electrolyte are significant, and cannot be neglected (see black curves). We also see that the bulk-MSA approach is slightly more accurate than the bulk-HNC model in predicting the depth in counterion distributions, although the position of the minimum is better captured by the bulk-HNC approach. Overall, both approaches

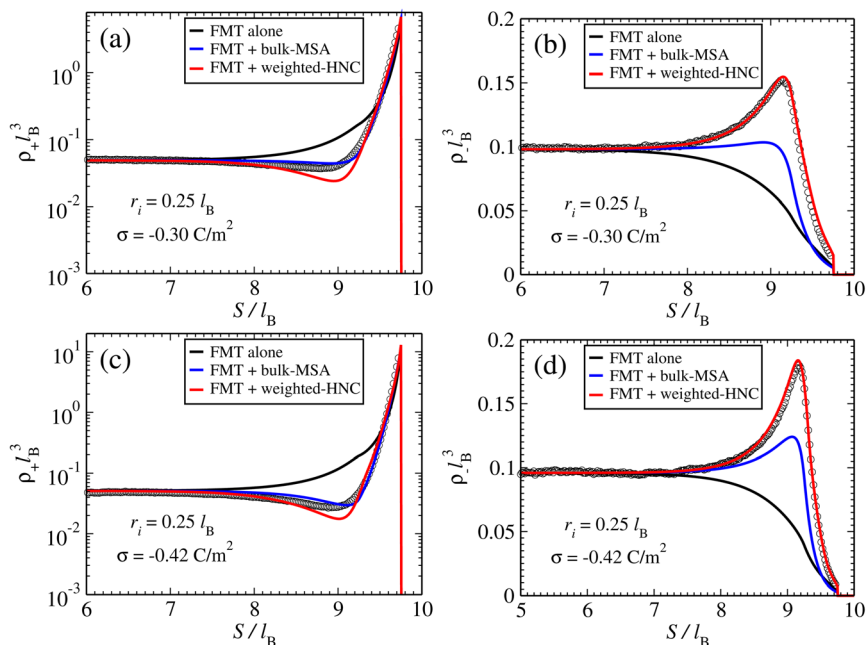


Fig. 2 Comparison between equilibrium ionic profiles of 2 : 1 electrolyte close to highly charged cylindrical surfaces, obtained using different DFT approaches and the results from DPD simulations (open circles). Blue lines are the results of the bulk-MSA expansion approach, while red curves are the predictions of the weighted-HNC approximation. In all cases, the ion size is fixed at  $r_i = 0.25 l_B$ . The upper panels show counterion (a) and coion (b) ionic distributions for a surface charge density of  $\sigma = -0.30 \text{ C m}^{-2}$ , whereas the lower panels show counterion (c) and coion (d) distributions for a pore-surface charge density  $\sigma = -0.42 \text{ C m}^{-2}$ .

perform reasonably well in predicting the counterion distributions. However, a large difference is observed when it comes to the coion distributions. In that case, the bulk-MSA approach is able to correctly predict the position of the peak in the anion distribution close to the charged wall. However, the height of the peak is clearly underestimated (see Fig. 2(b) and (d)). The proposed weighted-HNC approach is, on the other hand, able to accurately predict both the position and the height of the maximum of anion distribution. These results indicate that the proposed HNC approach can work as a promising alternative to the MSA-based theories in the presence of strong charge-layering effects. As we shall shortly see, this better agreement between theory and simulations is reflected in a more accurate prediction of the zeta potentials by the weighted-HNC approach, at least in cases where electrostatic correlations play a significant role in determining static ionic distributions.

## 5. Results

### 5.1 Monovalent electrolyte

In this section, we show results for the case of confined monovalent electrolyte. The fluid velocity profiles obtained from DPD simulations for various cylinder

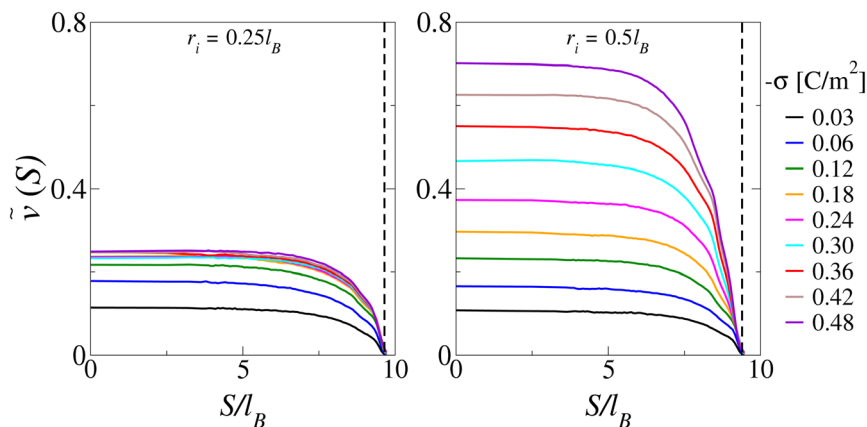


Fig. 3 Fluid velocity profiles for monovalent electrolyte solution considering two different ionic radii. The parameters are described in the text. The left and right panels show profiles for ionic radii  $r_i = 0.25l_B$  and  $r_i = 0.5l_B$ , respectively.

surface charge densities and two different ionic radii are shown in Fig. 3. It can be observed that, in the case of weakly charged surfaces, the fluid flow increases monotonically with the surface charge density. However, different qualitative behaviors are observed as the ionic size is changed. For a small ionic radius,  $r_i = 0.25l_B$ , the fluid flow is already saturated at  $\sigma = -0.18 \text{ C m}^{-2}$ . This is not the case for  $r_i = 0.5l_B$ , where the fluid flow continues to increase even at higher charge densities. This behavior may appear to be somewhat counter-intuitive since, at first sight, the stronger confinement in the case of larger ions might be expected to reduce the ionic mobility. According to Smoluchowski's equation, however, the steady state velocities at the cylinder center are proportional to the potential drop at this position with respect to the shear plane. Initially, an increase in surface charge leads to larger potential drops, which thus enhances ionic flow. However, as the surface charge increases beyond a certain threshold value, an increasingly large number of counterions will condense onto the shear plane, which effectively renormalizes the surface charge and saturates the zeta potential. This is not the case when the ionic size is increased. In this case, the ability of counterions to screen the surface charge is reduced by the packing constraints, preventing the condensation of a very large number of counterions within the shear plane. In order to clearly observe the saturation (monovalent counterions) and inversion (divalent counterions) of fluid flow, we plot the fluid velocity in the center of the pore,  $S = 0$ , as a function of surface charge density in Fig. 4. In the case of monovalent ions, the ionic size does not play a significant role for the fluid flow in the regime of weak to moderate surface charges ( $|\sigma| \leq 0.2 \text{ C m}^{-2}$ ). A significant size dependence, however, is observed for strongly charged pores. While for small ions the flow velocity saturates with the surface charge density, for large ions it increases linearly (Fig. 4, first panel).

Similar behavior is observed with the zeta potential. In previous DPD simulations of a pure DPD fluid,<sup>82</sup> the shear surface was found to be located at a distance  $0.1r_c$  from the channel surface. Since the hard-core repulsion prevents ions from coming closer than  $r_i$  to the pore surface, in the presence of counterions

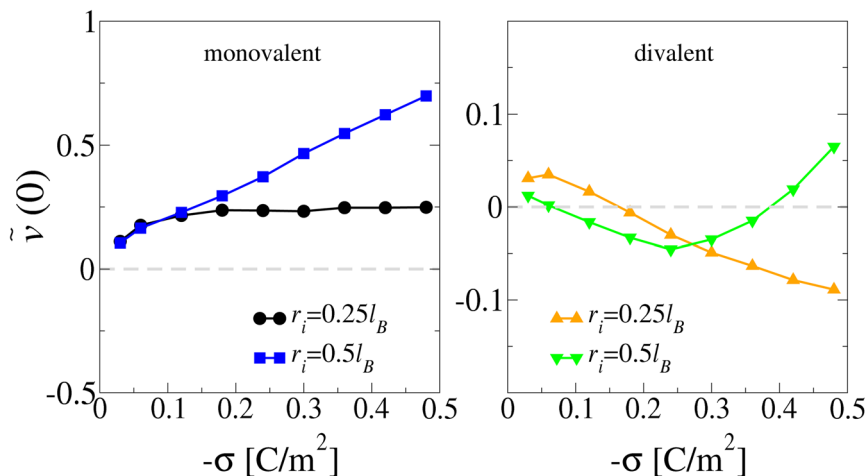


Fig. 4 Fluid velocity profiles in the middle of the nanopore as a function of charge density for various parameters. The left and right panels show profiles for monovalent and divalent ions, respectively.

we will define the shear plane to be located at  $S_{\text{sh}} = R - r_i - 0.1r_c$ . The zeta potential is then defined as the electrostatic potential at the location of the shear plane,  $\zeta = \phi(S_{\text{sh}})$ . This quantity is crucial for understanding the velocity profiles in the stationary regime and can be obtained using simulations, DFT, or the mean-field PB theory. Consider the electrostatic potential profiles, shown in Fig. 5. We observe that zeta potentials, in the case of smaller ions, achieve a saturation regime beyond which the dependence on the surface charge is very weak. On the other hand, for large ions, an unbound growth of the zeta potential is observed as the surface charge on the pore increases. This is consistent with the stationary flow observed in our DPD simulations. The Smoluchowski equation, eqn (4), can

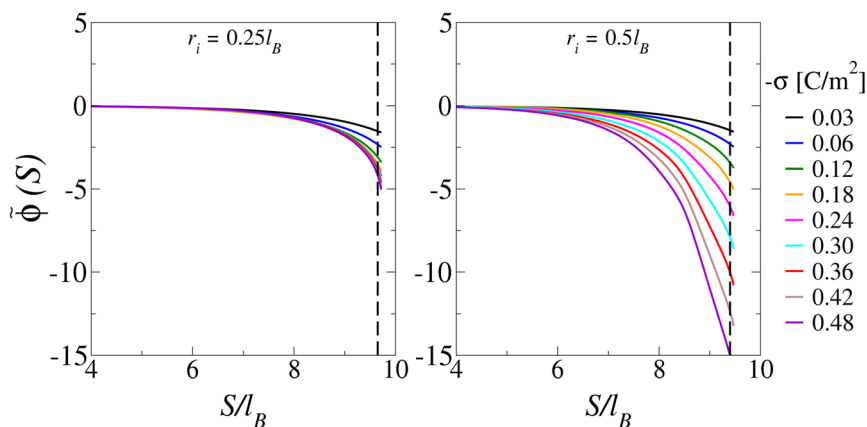


Fig. 5 Electrostatic potential inside a pore for 1 : 1 electrolyte solution for a stationary flow obtained from DPD simulations. Two different ionic radii are considered, as indicated in each panel. Further details about the considered parameters can be found in the text.

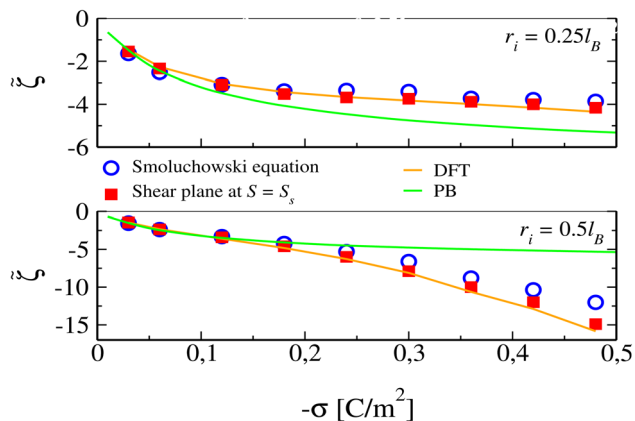


Fig. 6 Zeta potential as a function of surface charge density for monovalent electrolyte and two different ionic radii, as indicated in each panel. The parameters are described in text.

be used to relate the zeta potential to the fluid velocity obtained from simulations (Fig. 6, circles). Alternatively, it can be calculated directly from the electrostatic potential at the location of the shear plane (Fig. 6, squares). Knowledge of the location of the shear plane also allows us to use DFT or PB theory to predict the value of the zeta potential. In Fig. 6, we show the comparison between zeta potentials calculated using simulations, DFT, and PB mean-field theory. The DFT and PB perform well for low to moderate surface charge densities and small ions. The PB approach predicts the saturation of the zeta potential for large pore surface charge, which we clearly see not to be the case for large ions. On the other hand, the DFT works very well even for high surface charges and large ions. We also see that the calculations of the zeta potentials obtained using the fluid velocity at the center of the pore and the Smoluchowski equation agree reasonably well with the ones obtained from the equilibrium electrostatic potential at the shear plane. However a significant difference can be noticed for very large surface charge densities.

## 5.2 Divalent electrolyte

In Fig. 7, the fluid velocities for 2 : 1 electrolyte in pores with different surface charge densities are shown. For ions with radius  $r_i = 0.25l_B$ , the fluid flow reverses direction when  $|\sigma| > 0.18 \text{ C m}^{-2}$ . For such pores, more counterions condense near the pore surface than is necessary to neutralize the surface charge. This leads to the vanishing of the radial component of the electric field, indicating that the “effective” charge of the pore has reversed sign. In Fig. 8, we show the electrostatic potentials inside pores of different surface charge densities, containing 2 : 1 electrolyte. We can clearly see a highly non-monotonic behavior of the electrostatic potential, in contrast to the monotonic decay observed in Fig. 5. For 2 : 1 electrolyte inside pores with larger surface charge, the electrostatic potential develops a maximum close to the shear plane, indicating that the radial electric field vanishes at this position, signifying that charge reversal has taken place. On the other hand, for 1 : 1 electrolyte, the electric field only vanishes at the origin, so



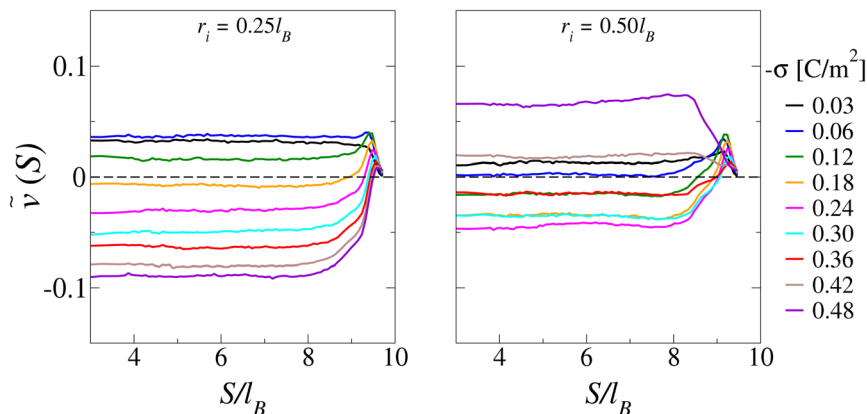


Fig. 7 Fluid velocity profiles for 2 : 1 electrolyte solution for ions of two different ionic size, as indicated in each panel. The parameters are described in the text.

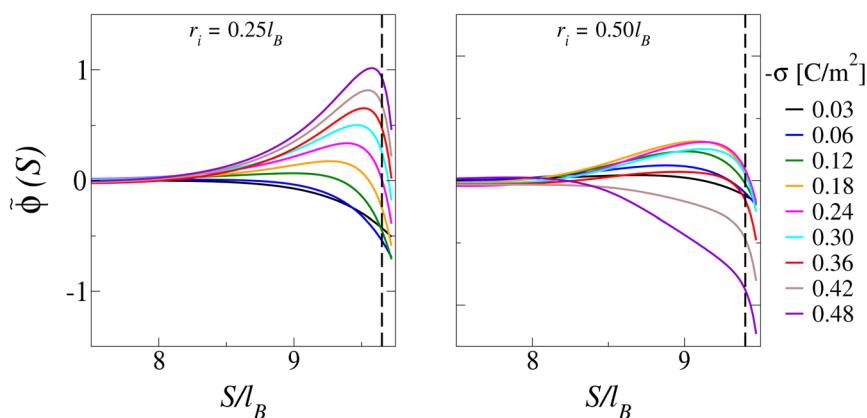


Fig. 8 Electrostatic potential profiles for divalent electrolyte solution considering two different ionic radii, as indicated in each panel. Details about the considered parameters are described in the text.

complete neutralization of the surface charge never takes place. Not all of the ions that are reversing the pore surface charge are within the shear plane and are truly “condensed”. This results in a very complex fluid flow, where close to the pore surface the fluid flows in one direction, but farther away it reverses the flow. For such complex flows, we find that the Smoluchowski equation is only semi-quantitatively correct. In particular, it does not precisely predict the location of the stagnation surface where the flow velocity vanishes – see Fig. 7.

Comparing Fig. 7 and 8, we see that the appearance of a maximum in the electrostatic potential can be associated with the reversal of the electroosmotic flow. Furthermore, we observe that for bigger ions with  $r_i = 0.5l_B$ , the reversal occurs even for relatively weakly charged pores,  $0.06 \text{ C m}^{-2} < |\sigma| < 0.4 \text{ C m}^{-2}$ . Note that the lower bound for the reversal of the electroosmotic flow in this case is 3 times smaller than for ions of radius  $r_i = 0.25l_B$ . On the other hand, for large ions

and  $|\sigma| > 0.4 \text{ C m}^{-2}$ , the flow reverses again, returning to the original direction. This behavior is a result of strong steric repulsion between large ions. For strongly charged pores, there is no space near the pore surface to pack a sufficient number of counterions necessary to neutralize or reverse the surface charge of the pore. On the other hand, the fact that large ions are more efficient than small ions at reversing the electroosmotic flow for weak-to-moderately charged pores, at first sight, appears very surprising. The explanation for this counterintuitive behavior is two-fold. The contact theorem allows us to relate the concentration of ions in contact with the surface to the osmotic pressure.<sup>148–151</sup> For the same number of ions, the pressure will be bigger for large ions than for small ones. This is due to electrostatic and steric correlations between the counterions and coions. When a counterion is in the bulk (far from the surface), its electric field is perfectly screened by the other ions of the electrolyte. This leads to favorable (negative) electrostatic solvation free energy.<sup>52</sup> When an ion moves to the surface, the screening cloud is deformed and the solvation free energy becomes less negative. Clearly the effect is much more important for small ions – when cations and anions can come in close to each other – than for large ions. Therefore, the electrostatic solvation free energy favors small ions to stay away from the surface more than large ions. In addition, the steric repulsion between the ions in the bulk raises the osmotic pressure of large ions, compared to the small ions at the same concentration – again favoring the expulsion of large ions towards the surface of the pore. These two mechanisms explain why, for the same bulk concentration and (small to moderate) surface charge density, larger counterions adsorb to the surface more than small ions.

Using the same location of the shear plane as for 1 : 1 electrolyte, we can once again calculate the value of the zeta potential from the stationary electrostatic potentials inside the pore. Alternatively, the zeta potential can be calculated using the Smoluchowski equation, eqn (4), and the fluid velocity at the center of the pore obtained from the DPD simulations. The results are shown in Fig. 9. The proposed DFT theory can also be applied to calculate the zeta potential considering the same shear-plane definition. All approaches (including the DFT in the context of the

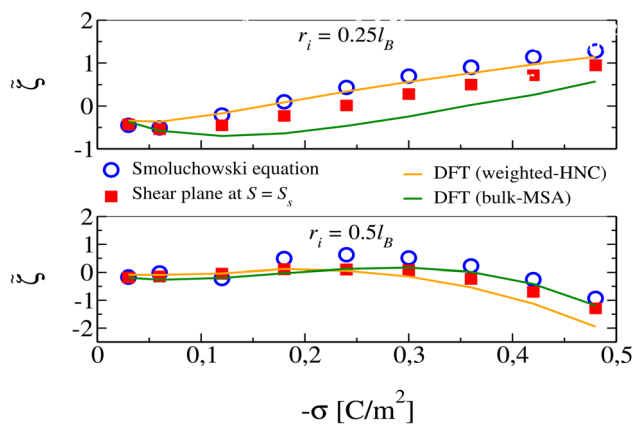
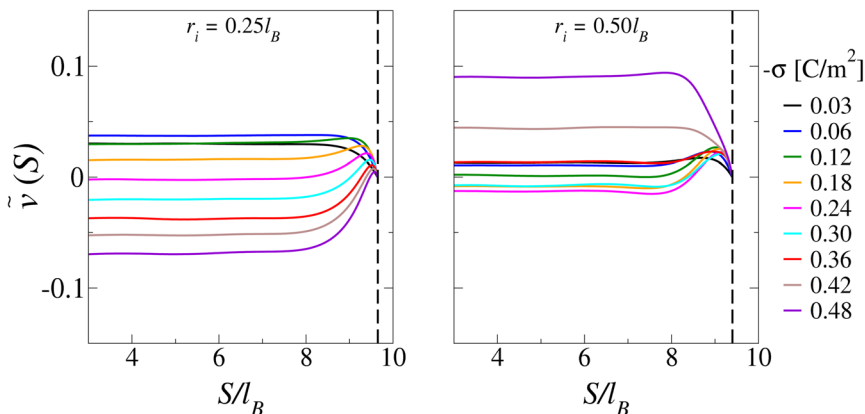


Fig. 9 Zeta potential as a function of the surface charge density for divalent electrolyte and two different ionic radii, as indicated in each panel. The remaining parameters under consideration are described in the text.



**Fig. 10** Velocity profiles for 2 : 1 electrolyte calculated using the Smoluchowski equation, eqn (4), with the electrostatic potential calculated directly from the simulations, for two different ionic radii as indicated in each panel. Although the fluid flow profiles are qualitatively similar to the ones observed in the DPD (Fig. 7), there are clear quantitative differences. In particular, note that the peak in velocity predicted by the Smoluchowski equation is significantly smaller than what we see in simulations. This clearly indicates the breakdown of the Smoluchowski equation for multivalent electrolyte solutions.

bulk-MSA approach) are compared in Fig. 9. From these results, it is clear that the proposed weighted-HNC approach performs better than the traditional bulk-MSA approximation in the case of smaller ions, where electrostatic correlations play a major role. On the other hand, the weighted-HNC approach becomes less accurate in the case of larger ion sizes and strongly charged surfaces. Such a lack of accuracy can most likely be attributed to the large averaging size of the weight function, which makes it difficult to capture strong local variations in the counterion distributions of large ions in close proximity to highly-charged surfaces. We also note that the agreement between zeta potentials calculated using the Smoluchowski equation and the shear plane can be improved by supposing that the shear plane moves farther away from the pore surface for highly charged pores. However, a more critical analysis indicates that for 2 : 1 electrolyte the Smoluchowski equation starts to break down. This is particularly evident when a complex two-layer flow takes place. If we use the exact stationary electrostatic potentials obtained from the DPD simulations to calculate the full velocity profiles using the Smoluchowski equation (eqn (4)) – see Fig. 10 – we find only a qualitative agreement. In particular, the peak in velocity close to the pore surface predicted by the Smoluchowski equation when reversal of the electroosmotic flow takes place is significantly smaller than what we see in simulations, indicating that in the case of 2 : 1 electrolytes the Smoluchowski equation is only qualitatively valid.

## 6. Conclusions

In this paper, we have studied the electroosmotic flow in charged nanopores with monovalent and divalent electrolyte with ions of two different sizes. The fluid flow depends strongly on ionic size and charge. This is due to strong steric and electrostatic correlations close to the charged surface. The zeta potential obtained

from the DPD simulations can also be calculated using either the PB equation or DFT, given the location of the shear plane. For low to moderate charge densities, in the case of small ionic size and monovalent electrolyte, both theoretical approaches are quite accurate. On the other hand, for large monovalent ions, the PB theory fails to predict the correct zeta potentials and corresponding electro-osmotic flow, while the DFT remains very accurate, even for highly charged surfaces. The zeta potential obtained using the Smoluchowski equation agrees reasonably well with the mean electrostatic potential at the shear surface, located slightly away from the contact plane, for both monovalent and divalent electrolytes. The proposed weighted-HNC DFT approach works well up to high surface charges, specially in the case of smaller ions, in which case its performance is shown to be better than MSA-based DFT approaches. In the case of large ions, the theory is only semi-quantitative when the channel surface charge becomes very high. This is partially due to packing effects which can not be properly described in the framework of the HNC approach. Moreover, the larger averaging sizes of the weighted-densities in the case of bigger ions close to highly-charged surfaces may underestimate the role of electrostatic correlations, thus requiring the need for different weighting approximations in this case. We also note that the Smoluchowski equation starts to break down for 2 : 1 electrolyte, predicting fluid velocity profiles that are significantly different from the ones observed in DPD simulations. In future work, it would be important to understand the mechanisms responsible for the breakdown of this important equation.

## Appendices

### Appendix A: FMT in cylindrical coordinates

In this Appendix, we shall present some details regarding the FMT implementation in cylindrical coordinates. To this end, we consider a system subject to an external potential which possess both azimuthal and longitudinal symmetries in a cylindrical coordinate system, as depicted in Fig. 11. As a consequence of rotational and translational invariances with respect to the longitudinal axis ( $z$ -axis), the resulting density profiles will depend only on the radial coordinate  $S$ , *i.e.*, the transversal distance from the  $z$ -axis. The quantities in FMT can be expressed as convolutions of the type

$$f(\mathbf{r}) = \int \omega(\mathbf{r} - \mathbf{r}') \rho(\mathbf{r}') d\mathbf{r}' \quad (\text{A1})$$

where  $\omega(\mathbf{r} - \mathbf{r}')$  are short-ranged functions which depend on the distance between source ( $\mathbf{r}'$ ) and observation ( $\mathbf{r}$ ) points. In order to numerically evaluate the above integral, it is convenient to consider (without loss of generality) a cylindrical coordinate system in which the observation point lies along the  $x$ -axis, as shown Fig. 11. In terms of Cartesian unit vectors  $\hat{e}_i$ , the observation and source points can be written as  $\mathbf{r} = S\hat{e}_x$  and  $\mathbf{r}' = S' \cos \varphi' \hat{e}_x + S' \sin \varphi' \hat{e}_y + z' \hat{e}_z$ , respectively, where  $(S', \varphi', z')$  denotes the set of cylindrical coordinates of point  $\mathbf{r}'$ . Defining  $\mathbf{R} = \mathbf{r} - \mathbf{r}'$  as the vector connecting observation and source points, it follows from this choice of reference frame that

$$\mathbf{R} = (S - S' \cos \varphi') \hat{e}_x - S' \sin \varphi' \hat{e}_y - z' \hat{e}_z \quad (\text{A2})$$

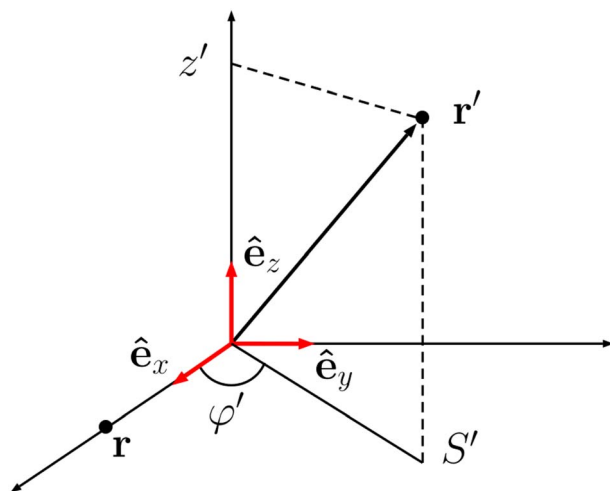


Fig. 11 Cylindrical coordinate system that has been set up for our FMT calculations. The observation point  $r$  lies along the  $x$ -axis, whereas the source points  $r'$  can be located anywhere.

The distance between observation and source points can thus be written in cylindrical coordinates as  $R = \sqrt{|\mathbf{R}|^2} = \sqrt{S^2 + S'^2 - 2SS' \cos \varphi' + z'^2} \equiv \sqrt{\tilde{R}^2 + z'^2}$ , where  $\tilde{R} \equiv |\mathbf{S} - \mathbf{S}'| = \sqrt{S^2 + S'^2 - 2SS' \cos \varphi'}$  is the transversal distance between these points, and can in the following be interpreted as an implicit function of  $S$ ,  $S'$  and  $\varphi'$ . Let us first consider the case in which  $\omega$  depends only on the distance between observation and source points, *i.e.*,  $\omega = \omega(R)$ . In this case, the integral eqn (A1) can be explicitly written as

$$f(S) = \int_0^\infty S' \rho(S') dS' \int_{-\pi}^\pi d\varphi' \int_{-\infty}^\infty \omega(R) dz', \quad (\text{A3})$$

where we have exploited the radial symmetry of the density distributions. Since  $R$  is an even function of both  $z'$  and  $\varphi'$ , the integrals above can be rewritten as

$$f(S) = 4 \int_0^\infty S' \rho(S') dS' \int_0^\pi d\varphi' \int_0^\infty \omega(R) dz', \quad (\text{A4})$$

where the factor of 4 accounts for the change in the lower integration limits. Now, the integral over  $z'$  can be converted into an integration over  $R$  *via* the substitution  $z' = \sqrt{R^2 - \tilde{R}^2}$ , which implies  $dz' = RdR/\sqrt{R^2 - \tilde{R}^2} = \frac{d}{dR} \left( \sqrt{R^2 - \tilde{R}^2} dR \right)$ . With this substitution, the function  $f(r)$  now reads

$$f(S) = 4 \int_0^\infty S' \rho(S') dS' \int_0^\pi d\varphi' \int_{\tilde{R}}^\infty \omega(R) \frac{d}{dR} \left( \sqrt{R^2 - \tilde{R}^2} \right) dR \quad (\text{A5})$$

Since the weight function  $\omega(R)$  vanishes beyond some cut-off distance  $R_c$ , the replacement  $\omega(R) \rightarrow \omega(R)\Theta(R_c - R)$  can be made above. Clearly,  $f(S)$  will be zero when  $\tilde{R} > R_c$ , as the last integral above spans a region where  $\omega(R)$  vanishes

identically. More precisely,  $f(S)$  will be non-zero for a given  $S$  only in regions  $(S', \varphi')$  in the transversal plane such that  $\tilde{R} \leq R_c$ . This condition limits the range of integration along the planar variables  $S'$  and  $\varphi'$ , which are constrained to satisfy:

$$\tilde{R}^2 = S^2 + S'^2 - 2SS'\cos\varphi' \leq R_c^2. \quad (\text{A6})$$

Since  $\cos\varphi'$  is limited to the range  $-1 \leq \cos\varphi' \leq 1$ , it is clear that the function  $\tilde{R} = |S - S'|$  has its range limited to the region  $|S - S'| \leq \tilde{R} \leq S + S'$ . Therefore, for points in the transversal plane in which  $R_c$  is larger than the upper bound of  $\tilde{R}$ , *i.e.*, such that  $S + S' \leq R_c$ , the condition above will be satisfied for all  $\varphi'$  in the range  $0 \leq \varphi' \leq \pi$ , in such a way that the limits of integration of  $\varphi'$  need not be changed in eqn (A5). Note that, since both  $S$  and  $S'$  are non-negative, this requirement can only be satisfied at observation points such that  $S < R_c$  (or, equivalently,  $|r| \leq R_c$ ). This condition implies that the integration over  $S'$  (when  $S < R_c$ ) can be performed over the range  $0 \leq S' \leq S - R_c$ , while the integration limits in  $\varphi'$  are kept unchanged. In the remaining interval  $(S - R_c \leq S' \leq S + R_c)$ , the upper bound in the  $\varphi'$  integration has to be changed in order to fulfil the condition in eqn (A6). This happens because, when  $S + S' > R_c$ , the fulfilment of the condition in eqn (A6) further requires that  $R_c$  should exceed the lower bound of  $|S - S'| < R_c$  (since otherwise  $\tilde{R} \leq R_c$  for all  $\varphi'$ ). In that case, the integral over  $S'$  should be limited to the range  $|S - S'| < R_c$ , *i.e.*,  $S - R_c \leq S \leq S + R_c$  if  $S > R_c$  and  $R_c - S \leq S \leq S + R_c$  when  $S < R_c$ . This means that the inequality in eqn (A6) will certainly be satisfied at the lower limit  $\varphi' = 0$ , but not at the upper bound where  $\varphi' = \pi$  (since  $S + S' > R_c$ ). As a consequence, there must be a maximum value of  $\varphi'$  within the range  $0 \leq \varphi' \leq \pi$ , up to which the condition in eqn (A6) is no longer fulfilled. The corresponding value of  $\varphi'_m$  is obviously the one that corresponds to the equality of both sides of eqn (A6), which leads to:

$$\varphi_m = \cos^{-1}\left(\frac{S^2 + S'^2 - R_c^2}{2SS'}\right) = \cos^{-1}\left(\frac{(S + S')^2 - R_c^2}{2SS'} - 1\right). \quad (\text{A7})$$

It is important to notice that the algebraic equation above is limited to situations where  $|S - S'| \leq R_c \leq S + S'$  (the case in which  $|S - S'| > R_c$  makes the integrand vanish identically, whereas the case  $S + S' > R_c \rightarrow S < R_c - S'$  has been discussed above). These conditions make sure that the quantity  $\frac{(S + S')^2 - R_c^2}{2SS'}$  is always limited within the range  $0 \leq \frac{(S + S')^2 - R_c^2}{2SS'} \leq 2$ , which guarantees that a real solution for  $\varphi_m$  in eqn (A7) can be found numerically.

In view of the above discussion, the integrals representing  $f(S)$  in the case of functions  $\omega(R)$  that vanish beyond a given cut-off distance  $R_c$  can be simplified as follows. In the situation where  $S < R_c$ , we have:

$$\begin{aligned} f(S) = & 4 \int_0^{R_c - S} \rho(S') S' dS' \int_0^\pi d\varphi' \int_{\tilde{R}}^{R_c} \omega(R) \frac{d}{dR} \left( \sqrt{R^2 - \tilde{R}^2} \right) dR \\ & + \int_{R_c - S}^{R_c + S'} \int_0^{\varphi_m} d\varphi' \int_{\tilde{R}}^{R_c} \omega(R) \frac{d}{dR} \left( \sqrt{R^2 - \tilde{R}^2} \right) dR, \quad (S \leq R_c), \end{aligned} \quad (\text{A8})$$

whereas in the region  $S > R_c$ , the function  $f(S)$  can be explicitly written as:

$$f(S) = 4 \int_{S-R_c}^{S+R_c} \rho(S') S' dS' \int_0^{\varphi_m} d\varphi' \int_{\tilde{R}}^{R_c} \omega(R) \frac{d}{dR} \left( \sqrt{R^2 - \tilde{R}^2} \right) dR \quad (S > R_c), \quad (\text{A9})$$

where  $\varphi_m$  is the solution of eqn (A7). Notice that the first term in eqn (A8) corresponds to the situation where  $S + S' < R_c$ , in which case condition eqn (A6) is satisfied for all values of  $\varphi'$ . It is also important to note that the upper integration limit  $S + R_c$  in the radial integrals is in practice to be replaced by  $\min(S + R_c, S_m)$ , where  $S_m$  is the maximum radial distance from the  $z$ -axis (e.g., where the system boundary is located). Finally, we mention that the integrals over  $R$  have been written in a format suitable for evaluation *via* integration by parts, once the functions  $\omega(R)$  are explicitly known.

We are now in a position to apply the above general results to obtain explicit integrals for the FMT weighted densities in eqn (8). The weighted densities  $n^{(\alpha)}(S)$  should now play the role of  $f(S)$  in eqn (A8) and (A9), while  $\omega(R)$  is to be replaced by the corresponding weighted densities, with cut-off distances  $R_c \rightarrow r_i$ . Let us start with  $\omega_i^{(3)}(R) = \Theta(r_i - R)$ . This case corresponds to the replacements  $\omega(R) \rightarrow 1$ ,  $R_c \rightarrow r_i$ , and  $f(S) \rightarrow n^{(3)}(R)$  (together with an implicit summation over all particle species  $i$ ). The integrals over  $R$  in eqn (A9) can be evaluated right away, yielding:

$$n^{(3)}(S) = 4 \sum_i \int_{S-r_i}^{S+r_i} \rho_i(S') S' dS' \int_0^{\varphi_m} d\varphi' \left[ \left( \sqrt{R^2 - \tilde{R}^2} \right) \right]_{\tilde{R}}^{r_i} \quad (S > r_i), \quad (\text{A10})$$

with similar relations holding for the case  $S \leq R_c = r_i$  in eqn (A8). Evaluating the upper and lower integration limits, we find:

$$\begin{aligned} n^{(3)}(S) &= 4 \sum_i \int_{S-r_i}^{S+r_i} \rho_i(S') S' dS' \int_0^{\varphi_m} d\varphi' \sqrt{r_i^2 - \tilde{R}^2} \\ &= 4 \sum_i \int_{S-r_i}^{S+r_i} \rho_i(S') S' dS' \int_0^{\varphi_m} d\varphi' \sqrt{r_i^2 - S^2 - S'^2 + 2SS' \cos \varphi'} \end{aligned} \quad (\text{A11})$$

Now, application of the trigonometric identity  $\cos \varphi' = 1 - 2 \sin^2(\varphi'/2)$  followed by a changing of variables  $\varphi = \varphi'/2 \rightarrow \varphi' = 2\varphi$  leads to:

$$n^{(3)}(S) = 8 \sum_i \int_{S-r_i}^{S+r_i} \rho_i(S') S' \sqrt{r_i^2 - (S - S')^2} dS' \underbrace{\int_0^{\varphi_m/2} d\varphi \sqrt{1 - k_i^2 \sin^2 \varphi}}_{E(k_i, \varphi_m/2)}, \quad (S > r_i), \quad (\text{A12})$$

where we have written the azimuthal angle integration in terms of the elliptic integral of the second kind  $E(k, \theta)$ , defined as:

$$E(\theta, k) = \int_0^\theta \sqrt{1 - k^2 \sin^2 \varphi} d\varphi, \quad (\text{A13})$$

where  $k_i \equiv \sqrt{\frac{4SS'}{r_i^2 - (S - S')^2}}$ . Since  $E(\theta, k)$  is defined to be a real-valued function,

the above definition implicitly implies that  $k^2 \sin^2 \theta \leq 1$  or, equivalently,  $k \leq 1/\sin \theta$ . To check whether this is indeed the case when  $\theta \rightarrow \varphi_m/2$  and

$k \rightarrow \sqrt{4SS'/[r_i^2 - (S - S')^2]}$ , we use eqn (A7) (with the substitution  $R_c \rightarrow r_i$ ) to evaluate the quantity  $\sin^2(\varphi_m/2)$  as:

$$\begin{aligned} \sin^2(\varphi_m/2) &= \frac{1}{2}(1 - \cos \varphi_m) = \frac{1}{2} \left( 2 + \frac{r_i^2 - (S + S')^2}{2SS'} \right) \\ &= \frac{r_i^2 - (S - S')^2}{4SS'} = \frac{1}{k_i^2}. \end{aligned} \quad (\text{A14})$$

We then conclude that  $k_i = 1/\sin(\varphi_m/2)$ . It is convenient, from a numerical point of view, to use this identity to define the coefficients  $k_i$  numerically. This is an important step during the numerical evaluation of the elliptic integrals, since very small numerical fluctuations in the evaluation of  $\varphi$  from eqn (A7) might render the square root in the definition of  $E(k, \theta)$  negative, leading to inconsistent results. Using these definitions, the weighted-density  $n^{(3)}(S)$  for  $S > R_c$  simplifies to:

$$n^{(3)}(S) = 8 \sum_i \int_{S-r_i}^{S+r_i} \rho_i(S') S' \sqrt{r_i^2 - (S - S')^2} E(k_i, \varphi_m/2) dS', \quad (S > r_i). \quad (\text{A15})$$

Similar calculations apply for the case  $S < R_c = r_i$  in eqn (A8), whereby the substitution  $\varphi_m \rightarrow \pi$  must be done in the first integral of eqn (A8), leading to:

$$\begin{aligned} n^{(3)}(S) &= 8 \int_0^{r_i-S} \rho_i(S') S' \sqrt{r_i^2 - (S - S')^2} E(k_i, \pi/2) dS' \\ &\quad + \int_{r_i-S}^{S+r_i} \rho_i(S') S' \sqrt{r_i^2 - (S - S')^2} E(k_i, \varphi_m/2) dS' \end{aligned} \quad (\text{A16})$$

We now proceed to the computation of the weight density  $n^{(2)}(S)$ , corresponding to the substitutions  $\omega(R) = \omega^{(2)}(R) = \delta(R - R_c)$  (with  $R_c = r_i$  and an implicit summation over particle competent  $i$ ) in eqn (A8) and (A9). Again, the integration over  $R$  can be performed straightforwardly, providing (for  $S > r_i$ ):

$$\begin{aligned} n^{(2)}(S) &= 4 \sum_i \int_{S-r_i}^{S+r_i} \rho_i(S') S' \int_0^{\varphi_m} d\varphi' \frac{d}{dR} \left( \sqrt{R^2 - \tilde{R}^2} \right)_{R=r_i} \\ &= 4 \sum_i r_i \int_{S-r_i}^{S+r_i} \rho_i(S') S' \int_0^{\varphi_m} \frac{d\varphi'}{\sqrt{r_i^2 - S^2 - S'^2 + 2SS' \cos \varphi'}}, \quad (S > r_i) \end{aligned} \quad (\text{A17})$$

Once again, we invoke the trigonometric identity  $\cos \varphi' = 1 - 2 \sin^2(\varphi'/2)$  and change variables from  $\varphi'$  to  $\varphi = 2\varphi'$ , such that the angular integration takes the form:

$$n^{(2)}(S) = 8 \sum_i \int_{S-r_i}^{S+r_i} \frac{\rho_i(S') S'}{\sqrt{r_i^2 - (S - S')^2}} dS' \underbrace{\int_0^{\varphi_m/2} \frac{d\varphi}{\sqrt{1 - k^2 \sin^2 \varphi}}}_{F(k_i, \varphi/2)}, \quad (S > r_i), \quad (\text{A18})$$



where now we have identified the angular integral with the elliptic integral of the first kind  $F(k, \theta)$ , defined as:

$$F(k, \theta) = \int_0^\theta \frac{d\varphi}{\sqrt{1 - k^2 \sin^2 \varphi}}, \quad (\text{A19})$$

where again the identifications  $\theta \rightarrow \varphi_m/2$  and  $k \rightarrow k_i = \sqrt{4SS'/[r_i^2 - (S - S')^2]} = 1/\sin(\varphi_m/2)$  have been made in eqn (A18), where  $\varphi_m$  is given by eqn (A7). The weighted function  $n^{(2)}$  is thus simplified to:

$$n^{(2)}(S) = 8 \sum_i \int_{S-r_i}^{S+r_i} \frac{\rho_i(S')S'}{\sqrt{r_i^2 - (S - S')^2}} F(k_i, \varphi_m/2) dS', \quad (S > r_i). \quad (\text{A20})$$

Proceeding along the same lines, it is easy to verify that in the region  $S < r_i$ , given by eqn (A8), the function  $n^{(2)}(S)$  takes the form:

$$n^{(2)}(S) = 8 \sum_i \int_0^{r_i-S} \frac{\rho_i(S')S'}{\sqrt{r_i^2 - (S - S')^2}} F(k_i, \pi/2) dS' + \int_{r_i-S}^{S+r_i} \frac{\rho_i(S')S'}{\sqrt{r_i^2 - (S - S')^2}} F(k_i, \varphi_m/2) dS', \quad (S < r_i). \quad (\text{A21})$$

Although the elliptic integrals  $F(k, \theta)$  and  $E(k, \theta)$  are defined as integrals over  $\varphi$ , it is important to notice that these functions can be efficiently computed through their power-series expansions, since recurrence relations among successive coefficients are known, allowing for a systematic and precise numerical evaluation of these functions.<sup>152</sup>

Let us now consider the third independent weight-function in the FMT formalism,  $\omega_i^{(2)}(R) = \delta(R - r_i)\hat{e}_R = -\nabla\omega_i^{(3)}(R)$ , which is a vector quantity. Here,  $\hat{e}_R = R/R$  is the unit vector connecting observation and source points. It is now convenient to go one step back and write each Cartesian component of  $\mathbf{n}^{(2)}(R)$  using eqn (A2) and (A3). The resulting components read as:

$$\mathbf{n}^{(2)} \cdot \tilde{\mathbf{e}}_x = \sum_i \int_0^\infty \rho_i(S')S' dS' \int_{-\pi}^\pi d\varphi' (S - S' \cos \varphi') \int_{-\infty}^\infty \frac{|\omega_i^{(2)}(R)|}{R} dz' \quad (\text{A22})$$

$$\mathbf{n}^{(2)} \cdot \tilde{\mathbf{e}}_y = \sum_i \int_0^\infty \rho_i(S')S'^2 dS' \int_{-\pi}^\pi d\varphi' \sin \varphi' \int_{-\infty}^\infty \frac{|\omega_i^{(2)}(R)|}{R} dz' \quad (\text{A23})$$

$$\mathbf{n}^{(2)} \cdot \tilde{\mathbf{e}}_z = \sum_i \int_0^\infty \rho_i(S')S'^2 dS' \int_{-\pi}^\pi d\varphi' \int_{-\infty}^\infty \frac{|\omega_i^{(2)}(R)|}{R} z' dz' \quad (\text{A24})$$

It is now clear from the above relations that the  $y$  and  $z$  components of  $\mathbf{n}^{(2)}$  vanish, since  $R$  is an even function of both  $\varphi'$  and  $z'$ , and thus the integration over these variables involves odd functions (for  $y$  and  $z$  components, respectively) in a symmetric interval, and therefore will vanish. This is not the case for the  $x$

component, since both integrations over  $\phi'$  and  $z'$  involve even functions of these variables. We then conclude that the vector  $\mathbf{n}^{(2)}$  points along the observation point direction  $\hat{\mathbf{e}}_r$  (which was chosen in such a way as to coincide with the  $x$ -axis). Again, the  $z'$  integration can be performed by changing variables to  $R = \sqrt{\tilde{R}^2 + z^2}$  (such that  $dz = RdR/z = RdR/\sqrt{R^2 - \tilde{R}^2}$ ). Substituting  $|\omega_i^{(2)}(R)| = \delta(r_i - R)$ , we find:

$$\mathbf{n}^{(2)}(S) = 4\hat{\mathbf{e}}_r \sum_i \int_0^\infty S' \rho_i(S') dS' \int_0^\pi (S - S' \cos \phi') \int_{\tilde{R}}^\infty \frac{\delta(r_i - R)}{\sqrt{R^2 - \tilde{R}^2}} dR, \quad (\text{A25})$$

where the factor of 4 arises from the change in the lower integration limits in  $\phi'$  and  $z'$ . As before, the integration over  $R$  vanishes unless  $\tilde{R} \leq R_c = R_i$ . As discussed above, this condition further restricts the ranges of integration in  $S'$  and  $\phi'$ , depending on whether  $S \leq r_i$  or  $S > r_i$ . Again, the arguments presented above carry over to this case as well. Therefore, for  $S > r_i$ , the expression above simplifies to:

$$\mathbf{n}^{(2)}(S) = 4\hat{\mathbf{e}}_r \sum_i \int_{S-r_i}^{S+r_i} S' \rho_i(S') dS' \int_0^{\phi_m} \frac{(S - S' \cos \phi')}{\sqrt{r_i^2 - \tilde{R}^2}} d\phi', \quad (\text{A26})$$

In order to evaluate the angular integration, we notice that the integrand in eqn (A26) can be written as:

$$\begin{aligned} \frac{(S - S' \cos \phi')}{\sqrt{r_i^2 - \tilde{R}^2}} &= \frac{1}{2S} \frac{(2S^2 - 2SS' \cos \phi')}{\sqrt{r_i^2 - \tilde{R}^2}} \\ &= \frac{1}{2S} \frac{\left( \overbrace{S^2 + S'^2 - 2SS' \cos \phi'}^{\tilde{R}^2} - r_i^2 + S^2 - S'^2 + r_i^2 \right)}{\sqrt{r_i^2 - \tilde{R}^2}} \\ &= \frac{1}{2S} \frac{(\tilde{R}^2 - r_i^2 + S^2 - S'^2 + r_i^2)}{\sqrt{r_i^2 - \tilde{R}^2}} = \frac{1}{2S} \left[ -\sqrt{r_i^2 - \tilde{R}^2} + \frac{S^2 - S'^2 + r_i^2}{\sqrt{r_i^2 - \tilde{R}^2}} \right]. \end{aligned} \quad (\text{A27})$$

Integrating both sides of the above expression in  $\phi'$  leads to:

$$\int_0^{\phi_m} \frac{(S - S' \cos \phi')}{\sqrt{r_i^2 - \tilde{R}^2}} d\phi' = \frac{1}{2S} \left( \begin{aligned} &2 \frac{S^2 - S'^2 + r_i^2}{\sqrt{r_i^2 - (S - S')^2}} \underbrace{\int_0^{\phi_m/2} \frac{d\phi}{\sqrt{1 - k_i^2 \sin^2 \phi}}}_{F(k_i, \phi_m/2)} \\ &- 2 \sqrt{r_i^2 - (S - S')^2} \underbrace{\int_0^{\phi_m/2} \sqrt{1 - k_i^2 \sin^2 \phi} d\phi}_{E(k_i, \phi_m/2)} \end{aligned} \right) \quad (\text{A28})$$

where the factor of 2 comes from the change of variable  $\varphi = 2\varphi'$  in the integrals. Again, we have identified the integrals over angles with elliptic integrals of the first and second kind. Replacing the above result into eqn (A26), we find:

$$\mathbf{n}^{(2)}(S) = \frac{4}{S} \hat{e}_i \sum_i \int_{S-r_i}^{S+r_i} S' \rho_i(S') \left[ \frac{\left( S^2 - S'^2 + r_i^2 \right)}{\sqrt{r_i^2 - (S - S')^2}} F(k_i, \varphi_m/2) - \sqrt{r_i^2 - (S - S')^2} E(k_i, \varphi_m/2) \right], \quad (\text{A29})$$

which is valid in the region  $S \geq r_i$ . Similarly, the calculations above can be equally applied to the case  $S < r_i$ , in which case one obtains:

$$\mathbf{n}^{(2)}(S) = \frac{4}{S} \hat{e}_i \sum_i \left[ \int_0^{r_i-S} S' \rho_i(S') \left( \frac{\left( S^2 - S'^2 + r_i^2 \right)}{\sqrt{r_i^2 - (S - S')^2}} F(k_i, \pi/2) - \sqrt{r_i^2 - (S - S')^2} E(k_i, \pi/2) \right) + \int_{r_i-S}^{r_i+S} S' \rho_i(S') \left( \frac{\left( S^2 - S'^2 + r_i^2 \right)}{\sqrt{r_i^2 - (S - S')^2}} F(k_i, \varphi_m/2) - \sqrt{r_i^2 - (S - S')^2} E(k_i, \varphi_m/2) \right) \right]. \quad (\text{A30})$$

Eqn (A15), (A16), (A20), (A21), (A29), and (A30) provide explicit integrals for the weighted-densities  $n^{(3)}(S)$ ,  $n^{(2)}(S)$  and  $\mathbf{n}^{(2)}(S)$  for all values of  $S$ . Since these integrals involve only the coordinate  $S'$ , and are performed over the range of a particle diameter, they can be easily evaluated numerically, once the functions  $\rho_i(S)$  are provided as input. The remaining weighted densities follow directly from the relations among the corresponding weighted functions, *i.e.*,  $\omega^{(1)}(R) = \omega^{(2)}(R)/(4\pi R)$ ,  $\omega^{(0)}(R) = \omega^{(2)}(R)/(4\pi R^2)$ , and  $\omega^{(1)}(R) = \omega^{(2)}(R)/(4\pi R)$ .

## Appendix B: residual correlations in the HNC approach

In this Appendix, a detailed derivation of eqn (17) is presented in the context of the proposed DFT-HNC approach. The model is based on a particle insertion method, in which a change in local chemical potential is considered when an ion is placed at a given location. To illustrate how the method works, we start by considering a change in free energy in an otherwise uniform system, driven by a given external potential that shifts the local concentrations by an amount  $\Delta\rho_i(\mathbf{r}) = \rho_i(\mathbf{r}) - \rho_i^0$ , where  $\rho_i^0$  are the uniform concentrations in the absence of the field. It is convenient to consider that the change in particle concentrations takes place continuously as the external field is “switched on” slowly from zero up to its final value. This is done by assigning the particle densities a parameter  $\lambda$  such that  $\rho_i(\mathbf{r}; \lambda = 0) = \rho_i^0$  and  $\rho_i(\mathbf{r}; \lambda = 1) = \rho_i(\mathbf{r})$ . If the concentrations are assumed to change across an equilibrium path, the one-to-one correspondence between equilibrium densities and applied field (assured by Henderson’s theorem<sup>153,154</sup>) implies that the coupling parameter  $\lambda$  can be equivalently thought of as a controlling

parameter of the field strength. When the coupling parameter  $\lambda$  is changed by a differential amount  $d\lambda$ , the density profiles undergo a change of  $d\rho(\mathbf{r}; \lambda) = \frac{\partial\rho(\mathbf{r}; \lambda)}{\partial\lambda}d\lambda$  at each point  $\mathbf{r}$ . Accordingly, the change in excess free energy is given by

$$d\mathcal{F}^{\text{ex}}(\lambda) = \sum_j \int \mu_j^{\text{ex}}(\mathbf{r}, \lambda) \frac{\partial\rho_j(\mathbf{r}; \lambda)}{\partial\lambda} d\lambda d\mathbf{r}, \quad (\text{B1})$$

where  $\mu_j^{\text{ex}} = \frac{\delta\mathcal{F}^{\text{ex}}}{\delta\rho_j(\mathbf{r}, \lambda)}$  is the excess chemical potential. Integrating both sides of this equation leads to the following exact relation for the free-energy change due to the applied field:

$$\Delta\mathcal{F}^{\text{ex}} \equiv \mathcal{F}^{\text{ex}} - \mathcal{F}_0^{\text{ex}} = \sum_j \int_0^1 d\lambda \int \mu_j^{\text{ex}}(\mathbf{r}; \lambda) \frac{\partial\rho_j(\mathbf{r}; \lambda)}{\partial\lambda} d\mathbf{r}, \quad (\text{B2})$$

where  $\mathcal{F}_0^{\text{ex}}$  is the free energy of the corresponding homogeneous system. Since the continuous path connecting initial and final states is arbitrary, we can take it to be of a linear dependence,  $\rho_j(\mathbf{r}; \lambda) = \rho_j^0 + \lambda\Delta\rho_j(\mathbf{r})$ . With this choice, the above relation is simplified to

$$\Delta\mathcal{F}^{\text{ex}} = \sum_j \int \Delta\rho_j(\mathbf{r}) d\mathbf{r} \int_0^1 d\lambda \int \mu_j^{\text{ex}}(\mathbf{r}; \lambda) d\lambda. \quad (\text{B3})$$

The excess chemical potential at coupling  $\lambda$  can be similarly obtained by considering the change in this quantity when  $\lambda$  is continuously changed from zero up to its actual value:

$$\Delta\mu_j^{\text{ex}}(\mathbf{r}; \lambda) = \mu_j^{\text{ex}}(\mathbf{r}; \lambda) - \mu_j^0 = -k_{\text{B}}T \sum_k \int_0^\lambda d\lambda' \int c_{jk}(\mathbf{r}, \mathbf{r}'; \lambda') \Delta\rho_k(\mathbf{r}') d\mathbf{r}', \quad (\text{B4})$$

where  $\mu_j^0 \equiv \mu_j^{\text{ex}}(\lambda = 0)$  is the excess chemical potential of the uniform system, and  $c_{jk}(\mathbf{r}, \mathbf{r}'; \lambda') = -\beta \frac{\delta\mu_j^{\text{ex}}(\mathbf{r}; \lambda')}{\delta\rho_k(\mathbf{r}'; \lambda')}$  are direct correlation functions. In principle, these quantities are to be computed for the inhomogeneous system, across the whole set of continuous coupling parameters. The HNC approach amounts to setting  $c_{jk}(\mathbf{r}, \mathbf{r}'; \lambda') = c_{jk}(|\mathbf{r} - \mathbf{r}'|)$ , where  $c_{jk}(|\mathbf{r} - \mathbf{r}'|)$  are the direct pair correlations for the uniform system (*i.e.*, at  $\lambda = 0$ ). Inserting this approximation into eqn (B4) and (B3) leads to the following expression for the excess free-energy change within the HNC approximation:

$$\Delta\mathcal{F}^{\text{ex}} = -\frac{k_{\text{B}}T}{2} \sum_{jk} \int c_{jk}(|\mathbf{r} - \mathbf{r}'|) \Delta\rho_j(\mathbf{r}) \Delta\rho_k(\mathbf{r}') d\mathbf{r} d\mathbf{r}', \quad (\text{B5})$$

where the particle conservation constraint  $\int \Delta\rho_i(\mathbf{r}) d\mathbf{r} = 0$  has been employed. This relation is similar to a mean-field approach, which is readily recovered when the direct correlations are replaced by their long-range counterparts,  $c_{jk}(|\mathbf{r} - \mathbf{r}'|) \rightarrow -\beta u_{jk}(|\mathbf{r} - \mathbf{r}'|)$ . Now, the total change in the grand potential when the field is turned on is  $\Delta\Omega = \Delta F^{\text{id}} + \Delta F^{\text{ex}} + \sum_j \rho_j(\mathbf{r}) (\phi_j(\mathbf{r}) - \mu_j) d\mathbf{r}$ . Therefore, in the context of the HNC approximation, the change in grand-potential induced by an external field is

$$\beta\Delta\Omega = \sum_j \int \rho_j(\mathbf{r}) [\log(\Lambda^3 \rho_j(\mathbf{r})) - 1 + \beta\phi_j(\mathbf{r}) - \beta\mu_j] d\mathbf{r} - \sum_j \int \rho_j^0 (\log(\Lambda^3 \rho_j^0) - 1 - \beta\mu_j) d\mathbf{r} - \frac{1}{2} \sum_{jk} \int c_{jk}(|\mathbf{r} - \mathbf{r}'|) \Delta\rho_j(\mathbf{r}) \Delta\rho_k(\mathbf{r}') d\mathbf{r} d\mathbf{r}'. \quad (\text{B6})$$

A straightforward application of the Euler-Lagrange condition  $\frac{\delta\Delta\Omega}{\delta\rho_j(\mathbf{r})} = 0$  in the above functional leads to the following equilibrium distributions:

$$\rho_j(\mathbf{r}) = \rho_j^0 \exp \left[ -\beta\phi_j(\mathbf{r}) + \sum_k \int c_{jk}(|\mathbf{r} - \mathbf{r}'|) \Delta\rho_k(\mathbf{r}') d\mathbf{r}' \right]. \quad (\text{B7})$$

Substitution of these equilibrium densities into eqn (B6) provides the total change in grand-potential induced by an external field:

$$\beta\Delta\Omega = \frac{1}{2} \sum_{jk} \int c_{jk}(|\mathbf{r} - \mathbf{r}'|) \Delta\rho_j(\mathbf{r}) \Delta\rho_k(\mathbf{r}') d\mathbf{r} d\mathbf{r}' + \rho_j^0 \sum_{jk} \int c_{jk}(|\mathbf{r} - \mathbf{r}'|) \Delta\rho_k(\mathbf{r}') d\mathbf{r} d\mathbf{r}' \quad (\text{B8})$$

These expressions are valid within the HNC framework, for external potentials  $\phi_j(\mathbf{r})$  of arbitrary sources. Now, we can take advantage of the Percus insertion method by choosing the potential source as an ion of species  $i$  located at point  $\mathbf{r}$ . In this case, the potential acting on a particle of type  $j$  at position  $\mathbf{r}'$ ,  $\phi_j(\mathbf{r}')$ , is to be recognized as the pair interaction  $u_{ij}(|\mathbf{r} - \mathbf{r}'|)$ , while the change in grand-potential can be identified as the chemical potential  $\mu_i(\mathbf{r})$  – the change in free energy upon inserting a particle of type  $i$  at position  $\mathbf{r}$ . Likewise, the density variations  $\Delta\rho_j(\mathbf{r}')$  are due to the polarization charges induced by ion insertion,  $\Delta\rho_j(\mathbf{r}') \rightarrow \rho_j^0(g_{ij}(|\mathbf{r} - \mathbf{r}'|) - 1) = \rho_j^0 h_{ij}(|\mathbf{r} - \mathbf{r}'|)$ . With these replacements, eqn (B7) becomes:

$$g_{ij}(\mathbf{r}) = \exp \left[ -\beta u_{ij}(\mathbf{r}) + \sum_k \rho_k^0 \int h_{ik}(\mathbf{r}') c_{kj}(|\mathbf{r} - \mathbf{r}'|) d\mathbf{r}' \right]. \quad (\text{B9})$$

This relation can be further simplified using the OZ equations for the uniform system,

$$\Gamma_{ij}(\mathbf{r}) \equiv h_{ij}(\mathbf{r}) - c_{ij}(\mathbf{r}) = \sum_k \rho_k^0 \int c_{ik}(|\mathbf{r} - \mathbf{r}'|) h_{kj}(\mathbf{r}') d\mathbf{r}'. \quad (\text{B10})$$

Replacement of eqn (B10) into (B8) leads to the traditional HNC closure relation for the bulk fluid:

$$g_{ij}(\mathbf{r}) = \exp(-\beta u_{ij}(\mathbf{r}) + \Gamma_{ij}(\mathbf{r})) \quad (\text{B11})$$

In the context of Percus insertion method, the change in free energy in eqn (B8) can be identified with the excess chemical potential related to the addition of a particle of type  $i$  at position  $\mathbf{r}$ . Under the substitutions  $\Delta\rho_j(\mathbf{r}') \rightarrow \rho_j^0 g_{ij}(\mathbf{r}')$  and  $\Delta\Omega$

→  $\mu_i^{\text{ex}}(\mathbf{r})$ , and making use of the OZ relation, eqn (B10), the excess chemical potential within the HNC formalism can be written as

$$\beta\mu_i^{\text{ex}} = \frac{1}{2} \sum_j \rho_j^0 \int h_{ij}(\mathbf{r}) \Gamma_{ij}(\mathbf{r}) d\mathbf{r} + \sum_j \rho_j^0 \int \Gamma_{ij}(\mathbf{r}) d\mathbf{r}. \quad (\text{B12})$$

Notice that, since the unperturbed system was uniform, the chemical potential does not depend on the particular point where the particle has been placed. In the case of coulombic interactions, it is convenient to split the direct correlations into short and long-range contributions,  $c_{ij}(\mathbf{r}) = c_{ij}^{\text{sr}}(\mathbf{r}) - l_{\text{B}}\alpha_i\alpha_j/r$  and  $\Gamma_{ij}^{\text{sr}}(\mathbf{r}) \equiv \Gamma_{ij}(\mathbf{r}) + l_{\text{B}}\alpha_i\alpha_j/r = h_{ij}(\mathbf{r}) - c_{ij}^{\text{sr}}(\mathbf{r})$ . The contributions  $c_{ij}^{\text{sr}}(\mathbf{r})$  come from short-range correlations, including hard-sphere interactions. The chemical potential in eqn (B12) can thus be re-written as:

$$\beta\mu_i^{\text{ex}} = \frac{1}{2} \sum_j \rho_j^0 \int h_{ij}(\mathbf{r}) \Gamma_{ij}^{\text{sr}}(\mathbf{r}) d\mathbf{r} + \sum_j \rho_j^0 \int \Gamma_{ij}^{\text{sr}}(\mathbf{r}) d\mathbf{r} - \alpha_i l_{\text{B}} \sum_j \rho_j^0 \alpha_j \int \left(1 + \frac{h_{ij}(\mathbf{r})}{2}\right) \frac{d\mathbf{r}}{r}. \quad (\text{B13})$$

The first term in the last integral vanishes due to the overall charge neutrality of the uniform system,  $\sum_j \rho_j^0 \alpha_j = 0$ , while the second term can be related to the correlation potential, *i.e.*, the change in the average electrostatic potential due to the polarizing cloud around the inserted ion,

$$\beta\Delta\psi_i = \sum_j \alpha_j l_{\text{B}} \int \frac{\Delta\rho_j(\mathbf{r})}{r} d\mathbf{r} = \sum_j l_{\text{B}} \alpha_j \rho_j^0 \int \frac{h_{ij}(\mathbf{r})}{r} d\mathbf{r}. \quad (\text{B14})$$

Note that, contrary to the mean-field potential (which vanishes in virtue of charge neutrality of the uniform fluid), the fluctuation potential takes account of electrostatic correlations in the bulk system. These contributions are naturally incorporated into the excess chemical potential in eqn (B13), along with the short-range steric correlations. Once these steric correlations are removed from eqn (B13), this quantity can be used to estimate the residual correlations in the inhomogeneous system. This can be done *via* a local approximation in which the bulk densities in eqn (B14) are replaced by their local values,  $\rho_j^0 \rightarrow \rho_j(\mathbf{r})$ . However, this approximation is known to be problematic for strongly inhomogeneous fluids. Therefore, a more suitable approach in these cases is to replace the bulk densities with the weighted densities  $n_i(\mathbf{r})$ , defined in eqn (20). Here, we propose a simple approach by considering a uniform weighting  $\omega_i(\mathbf{r}) = 3\Theta(r - R_i)/(4\pi R_i^3)$ , where the averaging radius is defined as  $R_i = (\sigma_i + 1/\kappa(\mathbf{r}))/2$ , where  $\sigma_i$  is the ionic diameter and  $1/\kappa(\mathbf{r}) = \left[4\pi l_{\text{B}} \sum_i \rho_i(\mathbf{r}) \alpha_i^2\right]^{-1/2}$  is the Debye length. Since the distance between two equally charged ions is expected to scale as  $\sim \sigma_i + 1/\kappa$ , the proposed averaging size can be interpreted as the excluded radius of a single ion (*i.e.*, half of the averaged ion-ion distance). Therefore, the chosen quantities  $R_i$  are typical distances that measure the decay of the polarization cloud around the center of an ion of radius  $r_i$ . The residual chemical potentials are then calculated as follows. First, a set of weighted-density profiles are computed starting from the

initial PB solution. The excess chemical potentials  $\mu_i^{\text{ex}}(\mathbf{r}) = \mu_i^{\text{ex}}(\{n_j(\mathbf{r})\})$  are then evaluated at each position  $\mathbf{r}$  by solving the OZ equation in Fourier space,

$$\tilde{T}_{ij}(\mathbf{k}) = \sum_k \tilde{h}_{ik}(\mathbf{k}) \tilde{c}_{kj}(\mathbf{k}), \quad (\text{B15})$$

where  $\tilde{T}_{ij}(\mathbf{k}) = \frac{\sqrt{n_i n_j}}{(2\pi)^{3/2}} \int T_{ij}(\mathbf{r}) e^{i\mathbf{k}\cdot\mathbf{r}} d\mathbf{r}$  (analogously for  $\hat{h}_{ij}(k)$  and  $\hat{c}_{ij}(k)$ ). This relation is supplemented by the HNC eqn (B11), yielding  $T_{ij}^{\text{sr}}(\mathbf{r}')$  and  $c_{ij}^{\text{sr}}(\mathbf{r}')$ , from which the excess chemical potentials can be evaluated *via* eqn (B13). Note that the local densities appearing in eqn (B14) do not satisfy electroneutrality near the pore surface. In order to avoid spurious divergences of chemical potentials, a uniform, structureless neutralizing background has to be included in the HNC chemical potentials eqn (B13), such that the mean-field electrostatic contribution in eqn (B13) vanishes. In a second step, the same HNC equations are solved considering the same weighted functions for a system of hard spheres ( $\alpha_i = 0$ ), from which the corresponding hard-sphere excess chemical potentials,  $\mu_{ij}^{\text{hs}}(\mathbf{r})$ , can be computed. Finally, the residual correlations for a given set of weighted densities are obtained from  $\mu_i^{\text{res}}(\mathbf{r}) = \mu_i^{\text{ex}}(\mathbf{r}) - \mu_i^{\text{hs}}(\mathbf{r})$ . These residual contributions are then used to obtain new profiles, along with improved estimates for the weight functions. The whole process is then repeated until a convergent solution is achieved.

## Conflicts of interest

There are no conflicts to declare.

## Acknowledgements

This work was supported by CAPES, CNPq, INCT-FCx, and FAPERGS.

## References

- 1 S. Pennathur and J. G. Santiago, *Anal. Chem.*, 2005, **77**, 6772.
- 2 J. R. Bordin, A. Diehl, M. C. Barbosa and Y. Levin, *Phys. Rev. E: Stat., Nonlinear, Soft Matter Phys.*, 2012, **85**, 031914.
- 3 U. Ghosh and S. Chakraborty, *Phys. Fluids*, 2015, **27**, 062004.
- 4 D. V. Melnikov, Z. K. Hulings and M. E. Gracheva, *Phys. Rev. E*, 2017, **95**, 063105.
- 5 K. Breitsprecher, M. Janssen, P. Srimuk, B. L. Mehdi, V. Presser, C. Holm and S. Kondrat, *Nat. Commun.*, 2020, **11**, 6085.
- 6 Y. Wang, Z. Hong, M. Wei and Y. Xia, *Adv. Funct. Mater.*, 2012, **22**, 5185.
- 7 R. Giridharagopal, J. Guo, J. Kong and D. S. Ginger, *ACS Appl. Mater. Interfaces*, 2021, **13**, 34616.
- 8 S. Joseph, R. J. Mashl, E. Jakobsson and N. R. Aluru, *Nano Lett.*, 2003, **3**, 1399.
- 9 P. M. Biesheuvel and M. Z. Bazant, *Phys. Rev. E*, 2016, **94**, 050601.
- 10 R. Peng, Y. Pan, Z. Li, S. Zhang, A. R. Wheeler, X. Tang and X. Liu, *Adv. Funct. Mater.*, 2020, **30**, 2003177.
- 11 M. Wang and S. Chen, *J. Colloid Interface Sci.*, 2007, **314**, 264.
- 12 A. Alizadeh, W.-L. Hsu, M. Wang and H. Daiguji, *Electrophoresis*, 2021, **42**, 834.

- 13 E. B. Kalman, I. Vlasiouk and Z. S. Siwy, *Adv. Mater.*, 2008, **20**, 293.
- 14 G. Yossifon and E. Demekhin, *Annu. Rev. Fluid. Mech.*, 2011, **44**, 401.
- 15 K. Xiao, L. Jiang and M. Antonietti, *Joule*, 2019, **3**, 2364.
- 16 K. Xiao, C. Wan, L. Jiang, X. Chen and M. Antonietti, *Adv. Mater.*, 2020, **32**, 2000218.
- 17 J. W. Polster, F. Aydin, J. P. de Souza, M. Z. Bazant, T. A. Pham and Z. S. Siwy, *J. Am. Chem. Soc.*, 2022, **144**, 11693.
- 18 A. Angelova, B. Angelov, S. Lesieur, R. Mutafchieva, M. Ollivon, C. Bourgaux, R. Willumeit and P. Couvreur, *J. Drug Delivery Sci. Technol.*, 2008, **18**, 41.
- 19 E. Moendarbary, T. Ng, H. Pan and K. Lam, *Microfluid. Nanofluid.*, 2010, **8**, 243.
- 20 S. J. Lippard, J. M. Berg and B. Roux, *Essays Biochem.*, 2017, **61**, 201.
- 21 Y. He, M. Tsutsui, Y. Zhou and X. S. Miao, *NPG Asia Mater.*, 2021, **13**, 48.
- 22 A. Arima, M. Tsutsui, T. Washio, Y. Baba and T. Kawai, *Anal. Chem.*, 2021, **93**, 215.
- 23 B. Hille, *Biophys. J.*, 1978, **22**, 283.
- 24 S. Marbach and L. Bocquet, *Chem. Soc. Rev.*, 2019, **48**, 3102.
- 25 H. Shao, Y.-C. Wu, Z. Lin, P.-L. Taberna and P. Simon, *Chem. Soc. Rev.*, 2020, **49**, 3005.
- 26 R. Amin, P. R. Kumar and I. Belharouak, in *Carbon Nanotubes*, ed. P. K. Ghosh, K. Datta and A. D. Rushi, IntechOpen, Rijeka, 2020, ch. 6.
- 27 S. Zhao, J. Xue and W. Kang, *J. Chem. Phys.*, 2013, **139**, 114702.
- 28 J. G. Gamaethiralalage, K. Singh, S. Sahin, J. Yoon, M. Elimelech, M. E. Suss, P. Liang, P. M. Biesheuvel, R. L. Zornitta and L. C. P. M. de Smet, *Energy Environ. Sci.*, 2021, **14**, 1095.
- 29 B. Corry, *J. Phys. Chem. B*, 2008, **112**, 1427.
- 30 D. Cohen-Tanugi and J. C. Grossman, *Nano Lett.*, 2012, **12**, 3602.
- 31 S. P. Surwade, S. N. Smirnov, I. V. Vlasiouk, R. R. Unocic, G. M. Veith, S. Dai and S. M. Mahurin, *Nat. Nanotechnol.*, 2015, **10**, 459.
- 32 C. J. Porter, J. R. Werber, M. Zhong, C. J. Wilson and M. Elimelech, *ACS Nano*, 2020, **14**, 10894.
- 33 S. Li, X. Zhang, Y. Liu and J. Su, *Phys. Chem. Chem. Phys.*, 2022, **24**, 13245.
- 34 Y. A. Perez Sirkin, M. Tagliacuzzi and I. Szleifer, *Mater. Today Adv.*, 2020, **5**, 100047.
- 35 J. Pods, J. Schönke and P. Bastian, *Biophys. J.*, 2013, **105**, 242.
- 36 B. Hille, *Prog. Biophys. Mol. Biol.*, 2022, **169–170**, 12.
- 37 R. Eisenberg, *Contemp. Phys.*, 1998, **39**, 447.
- 38 R. D. Keynes, The ionic channels in excitable membranes, in *Ciba Foundation Symposium 31 - Energy Transformation in Biological Systems*, John Wiley & Sons, Ltd, 1975, pp. 191–203, ch. 11.
- 39 B. Hille, *Biophys. J.*, 1978, **22**, 283.
- 40 W. Guan and M. A. Reed, *Nano Lett.*, 2012, **12**, 6441.
- 41 E. Gouaux and R. MacKinnon, *Science*, 2005, **310**, 1461.
- 42 H. Amiri, K. L. Shepard, C. Nuckolls and R. H. Sánchez, *Nano Lett.*, 2017, **17**, 1204.
- 43 P. Ma, J. Zheng, D. Zhao, W. Zhang, G. Lu, L. Lin, Z. Zhao, Z. Huang and L. Cao, *Materials*, 2021, **14**(22), 7012.
- 44 M. Zwolak, J. Lagerqvist and M. Di Ventra, *Phys. Rev. Lett.*, 2009, **103**, 128102.
- 45 S. Sahu, M. Di Ventra and M. Zwolak, *Nano Lett.*, 2017, **17**, 4719.



- 46 I. Sadeghi, P. Kaner and A. Asatekin, *Chem. Mater.*, 2018, **30**, 7328.
- 47 R. Epsztein, R. M. DuChanois, C. L. Ritt, A. Noy and M. Elimelech, *Nat. Nanotechnol.*, 2020, **15**, 426.
- 48 A. Naji, S. Jungblut, A. G. Moreira and R. R. Netz, *Physica A*, 2005, **352**, 131.
- 49 P. B. Peters, R. van Roij, M. Z. Bazant and P. M. Biesheuvel, *Phys. Rev. E*, 2016, **93**, 053108.
- 50 I. Palaia, I. M. Telles, A. P. dos Santos and E. Trizac, *Soft Matter*, 2020, **16**, 10688.
- 51 J. J. Nogueira and B. Corry, in *The Oxford Handbook of Neuronal Ion Channels*, Oxford University Press, 2019.
- 52 Y. Levin, *Rep. Prog. Phys.*, 2002, **65**, 1577.
- 53 J. P. Hansen and I. R. McDonald, *Theory of Simple Liquids*, Academic Press, London, 2006.
- 54 M. Lozada-Cassou, in *Fundamentals of Inhomogeneous Fluids*, ed. D. Henderson, Marcel Dekker, New York, 1992.
- 55 J. N. Israelachvili, in *Intermolecular and Surface Forces*, Academic Press, Boston, 3rd edn, 2011.
- 56 F. H. J. van der Heyden, D. J. Bonthuis, D. Stein, C. Meyer and C. Dekker, *Nano Lett.*, 2007, **7**, 1022.
- 57 S. Pennathur, *Lab Chip*, 2008, **8**, 383.
- 58 A. Szymczyk, H. Zhu and B. Balannec, *Langmuir*, 2010, **26**, 1214.
- 59 H. Daiguji, P. Yang and A. Majumdar, *Nano Lett.*, 2004, **4**, 137.
- 60 Y. Levin, *Europhys. Lett.*, 2006, **76**, 163.
- 61 M. M. Hatlo, D. Panja and R. van Roij, *Phys. Rev. Lett.*, 2011, **107**, 068101.
- 62 Y. Jing, V. Jadhao, J. W. Zwanikken and M. O. de la Cruz, *J. Chem. Phys.*, 2015, **143**, 194508.
- 63 H. Antila and E. Luijten, *Phys. Rev. Lett.*, 2018, **120**, 135501.
- 64 I. M. Telles and A. P. dos Santos, *Langmuir*, 2021, **37**, 2104.
- 65 R.-J. Yang, L.-M. Fu and Y.-C. Lin, *J. Colloid Interface Sci.*, 2001, **239**, 98.
- 66 P. P. Ewald, *Ann. Phys.*, 1921, **369**, 253.
- 67 I. C. Yeh and M. L. Berkowitz, *J. Chem. Phys.*, 1999, **111**, 3155.
- 68 A. P. dos Santos, M. Giroto and Y. Levin, *J. Chem. Phys.*, 2016, **144**, 144103.
- 69 R. D. Groot and P. B. Warren, *J. Chem. Phys.*, 1997, **107**, 4423.
- 70 J. Smiatek, M. Sega, C. Holm, U. D. Schiller and F. Schmid, *J. Chem. Phys.*, 2009, **130**, 244702.
- 71 F. J. Solis, G. Vernizzi and M. O. de la Cruz, *Soft Matter*, 2011, **7**, 1456.
- 72 A. P. dos Santos, M. Giroto and Y. Levin, *J. Chem. Phys.*, 2017, **147**, 184105.
- 73 I. M. Telles, R. K. Bombardelli, A. P. dos Santos and Y. Levin, *J. Mol. Liq.*, 2021, **336**, 116263.
- 74 R. K. Bombardelli, I. M. Telles, A. P. dos Santos and Y. Levin, *J. Phys. Chem. B*, 2021, **125**, 11091.
- 75 H. Li, S. Wei, C. Qing and J. Yang, *J. Colloid Interface Sci.*, 2003, **258**, 40.
- 76 R. J. Hunter, *Zeta Potential in Colloid Science : Principles and Applications*, *Colloid Science*, Academic Press, London, 1988.
- 77 W. B. Russel, D. A. Saville and W. R. Schowalter, *Colloidal Dispersions*, *Cambridge Monographs on Mechanics*, Cambridge University Press, Cambridge, 1989.
- 78 E. Klaseboer and D. Y. Chan, *J. Colloid Interface Sci.*, 2020, **568**, 176.

- 79 I. Semenov, S. Raafatnia, M. Sega, V. Lobaskin, C. Holm and F. Kremer, *Phys. Rev. E: Stat., Nonlinear, Soft Matter Phys.*, 2013, **87**, 022302.
- 80 S. Pianegonda, M. Barbosa and Y. Levin, *Europhys. Lett.*, 2005, **71**, 831.
- 81 A. Diehl and Y. Levin, *J. Chem. Phys.*, 2006, **125**, 054902.
- 82 I. M. Telles, Y. Levin and A. P. dos Santos, *Langmuir*, 2022, **38**, 3817.
- 83 P. Grochowski and J. Trylska, *Biopolymers*, 2008, **89**, 93.
- 84 T. J. Robbins, J. D. Ziebarth and Y. Wang, *Biopolymers*, 2014, **101**, 834.
- 85 P. Batys, S. Luukkonen and M. Sammalkorpi, *Phys. Chem. Chem. Phys.*, 2017, **19**, 24583.
- 86 V. Dorvilien, C. Patra, L. Bhuiyan and C. Outhwaite, *Condens. Matter Phys.*, 2013, **16**, 43801.
- 87 A. G. Moreira and R. R. Netz, *Europhys. Lett.*, 2000, **52**, 705.
- 88 L. Bocquet, E. Trizac and M. Aubouy, *J. Chem. Phys.*, 2002, **117**, 8138.
- 89 E. Trizac, L. Bocquet and M. Aubouy, *Phys. Rev. Lett.*, 2002, **89**, 248301.
- 90 S. Zhou, S. Lamperski and M. Sokołowska, *J. Stat. Mech.: Theory Exp.*, 2017, **2017**, 073207.
- 91 R. Evans, in *Fundamentals of Inhomogeneous Fluids*, ed. D. Henderson, Marcel Dekker, New York, 1992.
- 92 R. Evans, *Adv. Phys.*, 1979, **28**, 143.
- 93 J. Wu and Z. Li, *Annu. Rev. Phys. Chem.*, 2007, **58**, 85.
- 94 J. Wu, T. Jiang, D. en Jiang, Z. Jin and D. Henderson, *Soft Matter*, 2011, **7**, 11222.
- 95 M. Vrugt and R. Wittkowski, *J. Phys.: Condens. Matter*, 2022, **35**, 041501.
- 96 F. van Swol and J. R. Henderson, *Phys. Rev. A*, 1991, **43**, 2932.
- 97 G. Kahl and H. Löwen, *J. Phys.: Condens. Matter*, 2009, **21**, 464101.
- 98 A. Dreuw, *ChemPhysChem*, 2006, **7**, 2259.
- 99 K. Capelle, *Braz. J. Phys.*, 2006, **36**, 1318.
- 100 M. Barhoumi, *The Density Functional Theory and beyond: Example and Applications*, IntechOpen, 2021.
- 101 A. P. Hughes, U. Thiele and A. J. Archer, *Am. J. Phys.*, 2014, **82**, 1119.
- 102 P. Cats, S. Kuipers, S. D. Wind, R. V. Damme, G. M. Coli, M. Dijkstra and R. V. Roij, *APL Mater.*, 2021, **9**, 031109.
- 103 A. P. dos Santos, Y. Uematsu, A. Rathert, P. Loche and R. R. Netz, *J. Chem. Phys.*, 2020, **153**, 034103.
- 104 L. Tociu, G. Rassolov, É. Fodor and S. Vaikuntanathan, *J. Chem. Phys.*, 2022, **157**, 014902.
- 105 Y. Rosenfeld, M. Schmidt, H. Löwen and P. Tarazona, *Phys. Rev. E: Stat. Phys., Plasmas, Fluids, Relat. Interdiscip. Top.*, 1997, **55**, 4245.
- 106 Y. Rosenfeld, *J. Phys.: Condens. Matter*, 2002, **14**, 9141.
- 107 R. Roth, *J. Phys.: Condens. Matter*, 2010, **22**, 063102.
- 108 P. Tarazona, *Phys. Rev. Lett.*, 2000, **84**, 694.
- 109 R. Roth, R. Evans, A. Lang and G. Kahl, *J. Phys.: Condens. Matter*, 2002, **14**, 12063.
- 110 Y.-X. Yu and J. Wu, *J. Chem. Phys.*, 2002, **117**, 10156.
- 111 J. A. Cuesta, Y. Martínez-Ratón and P. Tarazona, *J. Phys.: Condens. Matter*, 2002, **14**, 11965.
- 112 V. Callewaert, R. Saniz, B. Barbiellini, A. Bansil and B. Partoens, *Phys. Rev. B*, 2017, **96**, 085135.
- 113 R. D. Groot, *J. Chem. Phys.*, 1991, **95**, 9191.

- 114 A. R. Denton and N. W. Ashcroft, *Phys. Rev. A*, 1991, **44**, 8242.
- 115 A. Diehl, M. N. Tamashiro, M. C. Barbosa and Y. Levin, *Physica A*, 1999, **274**, 433.
- 116 R. Roth and D. Gillespie, *J. Phys.: Condens. Matter*, 2016, **28**, 244006.
- 117 T. Biben, J. Hansen and J. Barrat, *J. Chem. Phys.*, 1993, **98**, 7330.
- 118 M. C. Barbosa, M. Deserno and C. Holm, *Europhys. Lett.*, 2000, **52**, 80.
- 119 M. Giroto, A. P. dos Santos, T. Colla and Y. Levin, *J. Chem. Phys.*, 2014, **141**, 014106.
- 120 D. Gillespie, W. Nonner and R. S. Eisenberg, *Phys. Rev. E: Stat., Nonlinear, Soft Matter Phys.*, 2003, **68**, 031503.
- 121 D. Gillespie, M. Valiskó and D. Boda, *J. Phys.: Condens. Matter*, 2005, **17**, 6609.
- 122 J. Jiang, V. V. Ginzburg and Z.-G. Wang, *Soft Matter*, 2018, **14**, 5878.
- 123 J. W. Cahn, *J. Chem. Phys.*, 1977, **66**, 3667.
- 124 Z. Li and J. Wu, *Phys. Rev. E: Stat., Nonlinear, Soft Matter Phys.*, 2004, **70**, 031109.
- 125 J. Wu, *AIChE J.*, 2006, **52**, 1169.
- 126 J. Wu, Classical density functional theory for molecular systems, in *Variational Methods in Molecular Modeling*, ed. J. Wu, Springer Singapore, Singapore, 2017, pp. 65–99.
- 127 J.-P. Simonin, *AIP Adv.*, 2020, **10**, 095213.
- 128 J.-P. Simonin and J. S. Høye, *J. Chem. Phys.*, 2021, **155**, 114502.
- 129 E. Waisman, D. Henderson and J. L. Lebowitz, *Mol. Phys.*, 1976, **32**, 1373.
- 130 J.-P. Simonin, O. Bernard and L. Blum, *Oil Gas Sci. Technol.*, 2008, **63**, 321.
- 131 J. Krejčí, I. Nezbeda, R. Melnyk and A. Trokhymchuk, *Condens. Matter Phys.*, 2012, **14**(3), 33005.
- 132 S. Hlushak, A. Trokhymchuk and I. Nezbeda, *Condens. Matter Phys.*, 2012, **14**(3), 33004.
- 133 L. M. Varela, J. M. Ruso, M. Garcia and V. Mosquera, *J. Chem. Phys.*, 2000, **113**, 10174.
- 134 Y. Tang, *J. Chem. Phys.*, 2003, **118**, 4140.
- 135 S. P. Hlushak, P. A. Hlushak and A. Trokhymchuk, *J. Chem. Phys.*, 2013, **138**, 164107.
- 136 P. H. Fries and G. N. Patey, *J. Chem. Phys.*, 1985, **82**, 429.
- 137 P. Bandyopadhyay and P. Gupta-Bhaya, *Chem. Phys. Lett.*, 2019, **732**, 136664.
- 138 F. S. Carvalho and J. P. Braga, *J. Braz. Chem. Soc.*, 2021, **32**, 2257.
- 139 M. Oettel, *J. Phys.: Condens. Matter*, 2005, **17**, 429.
- 140 J. Wu, *AIChE J.*, 2006, **52**, 1169.
- 141 R. M. Levy, D. Cui, B. W. Zhang and N. Matubayasi, *J. Phys. Chem. B*, 2017, **121**, 3825.
- 142 I. Pivkin and G. Karniadakis, *J. Comput. Phys.*, 2005, **207**, 114.
- 143 A. Ahmed and R. Sadus, *Phys. Rev. E: Stat., Nonlinear, Soft Matter Phys.*, 2009, **80**, 061101.
- 144 M. P. Allen and D. J. Tildesley, *Computer Simulations of Liquids*, Oxford University Press, Oxford, 1987.
- 145 J. Smiatek, M. Allen and F. Schmid, *Eur. Phys. J. E*, 2008, **26**, 115.
- 146 G. A. Mansoori, N. F. Carnahan, K. E. Starling and T. W. Leland, *J. Chem. Phys.*, 1971, **54**, 1523.
- 147 K. Ng, *J. Chem. Phys.*, 1974, **61**, 2680.

- 148 S. L. Carnie, D. Y. C. Chan, D. J. Mitchell and B. W. Ninham, *J. Chem. Phys.*, 1981, **74**, 1472.
- 149 M. Lozada-Cassou, *J. Chem. Phys.*, 1984, **80**, 3344.
- 150 J. P. Mallarino, G. Téllez and E. Trizac, *Mol. Phys.*, 2015, **113**, 2409.
- 151 M. Holovko, V. Vlachy and D. di Caprio, *J. Mol. Liq.*, 2023, **371**, 121040.
- 152 W. H. Press, S. A. Teukolsky, W. T. Vetterling and B. P. Flannery, Numerical Recipes in FORTRAN, *The Art of Scientific Computing*, Cambridge University Press, USA, 2nd edn, 1992.
- 153 R. L. Henderson, *Phys. Lett. A*, 1974, **49**, 197.
- 154 A. P. Lyubartsev and A. Laaksonen, *Phys. Rev. E: Stat., Nonlinear, Soft Matter Phys.*, 1995, **52**, 3730.